

# Nanoscale

Accepted Manuscript



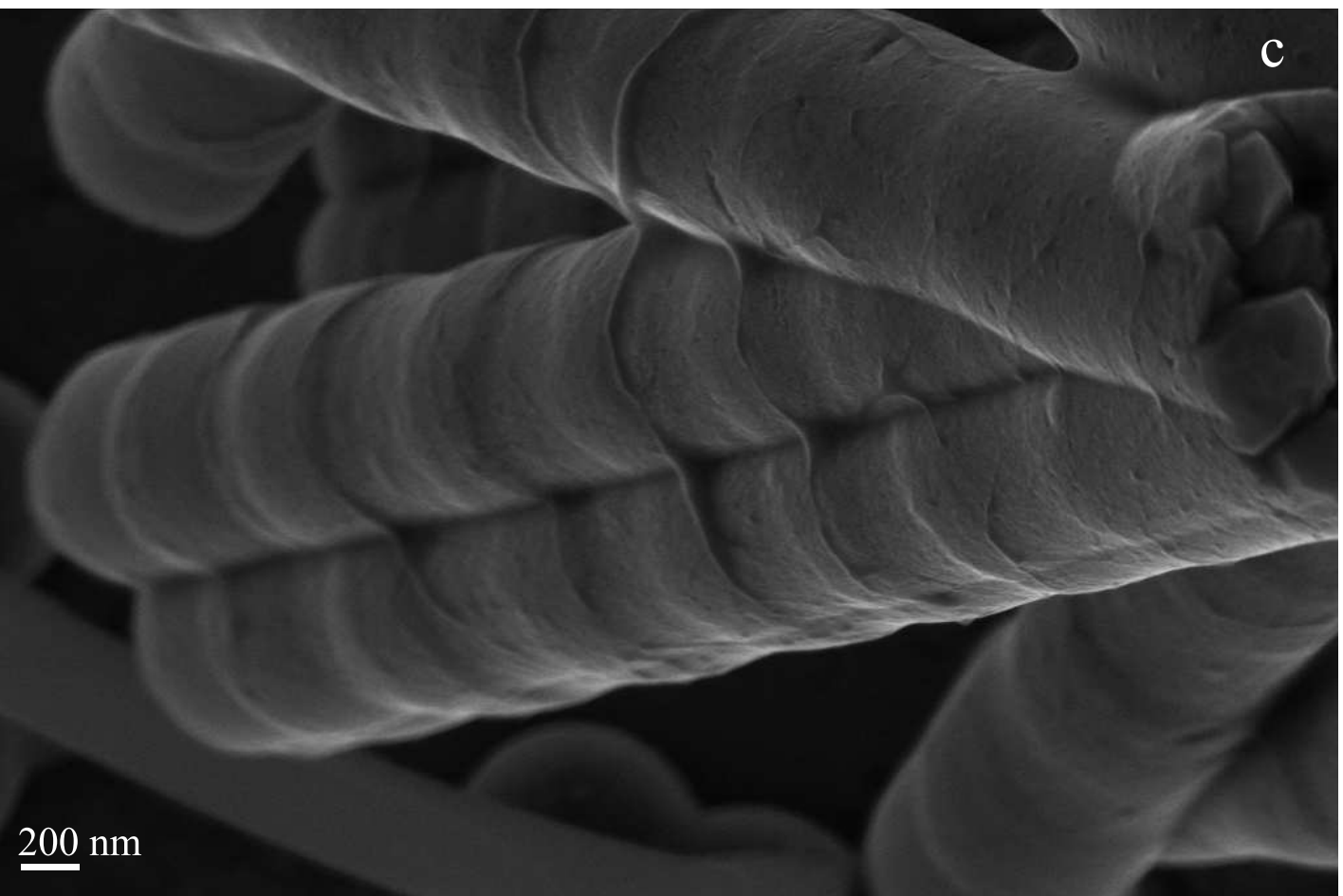
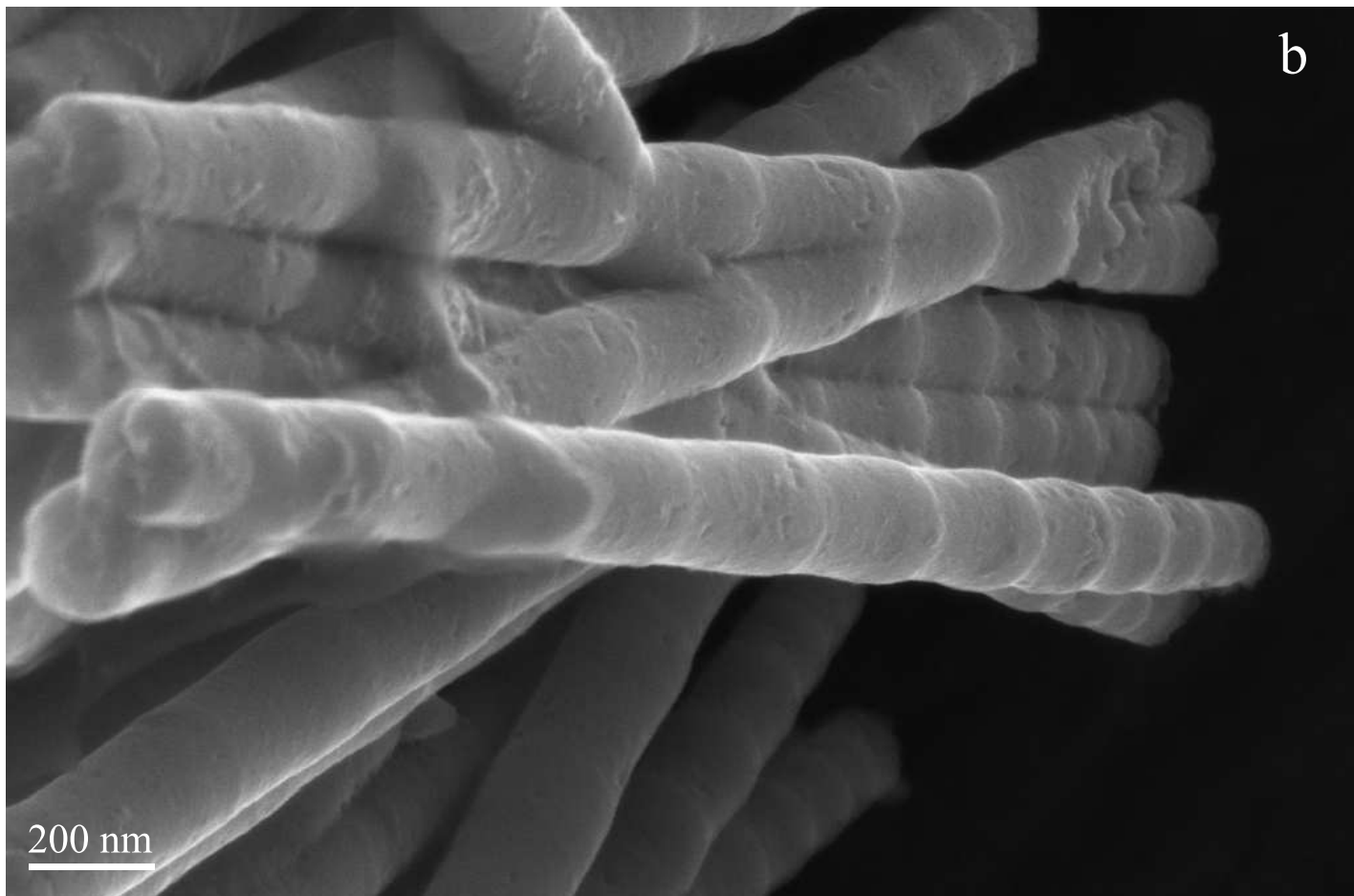
This is an *Accepted Manuscript*, which has been through the Royal Society of Chemistry peer review process and has been accepted for publication.

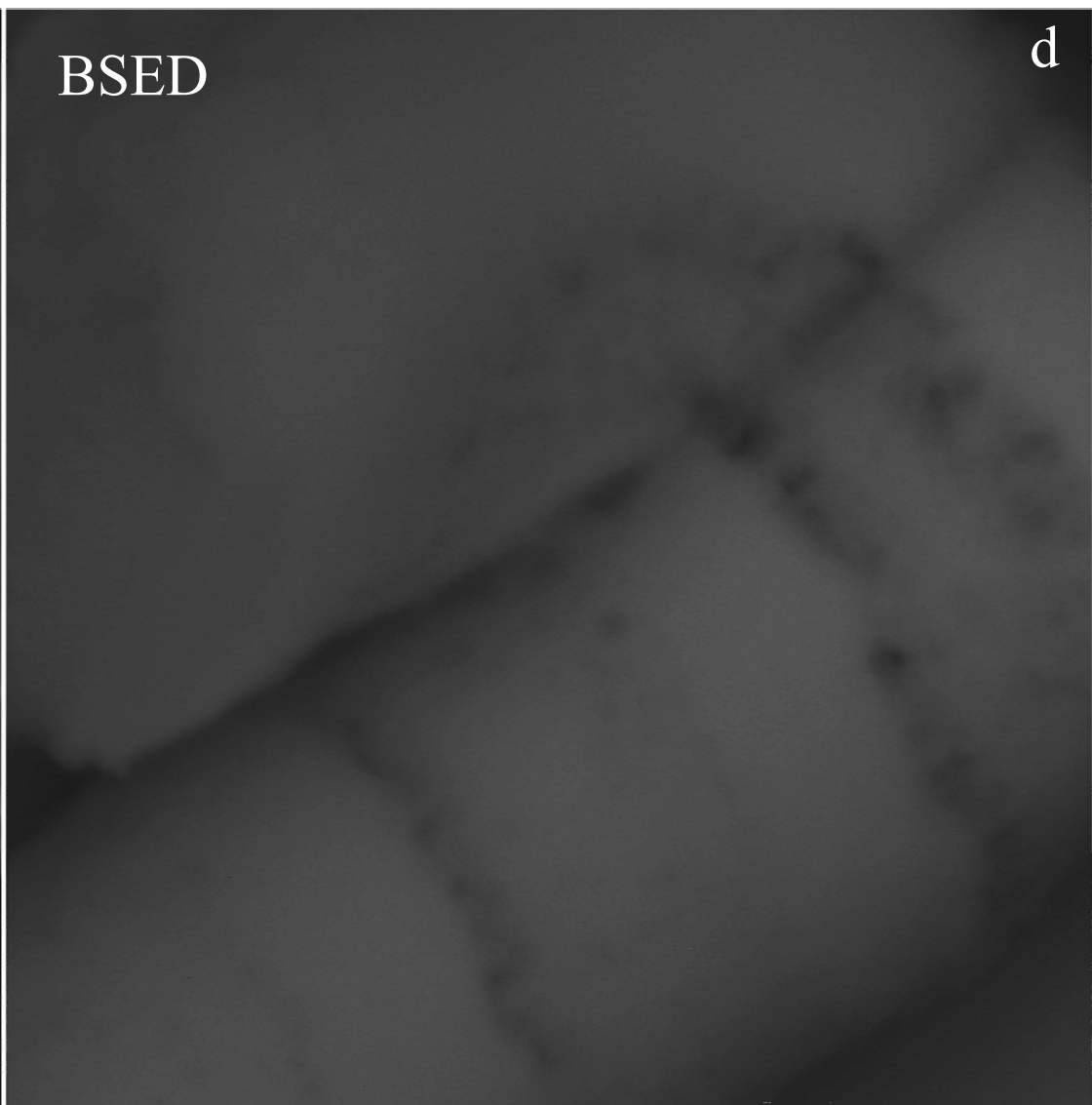
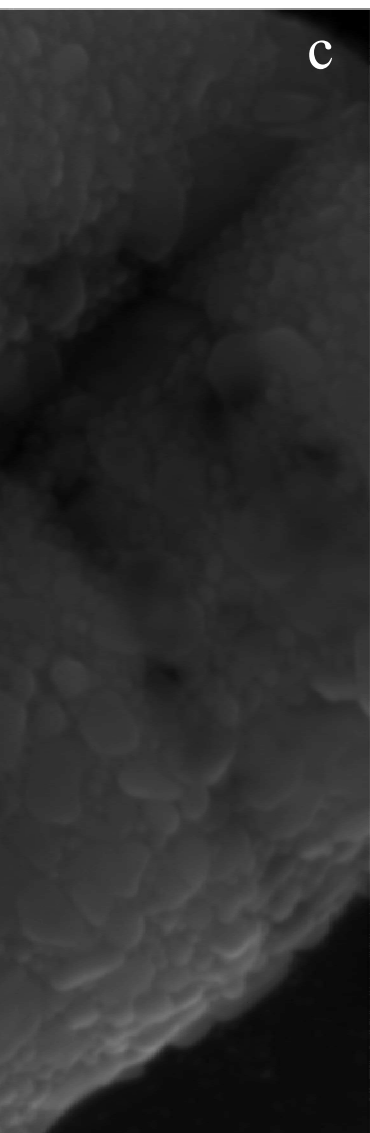
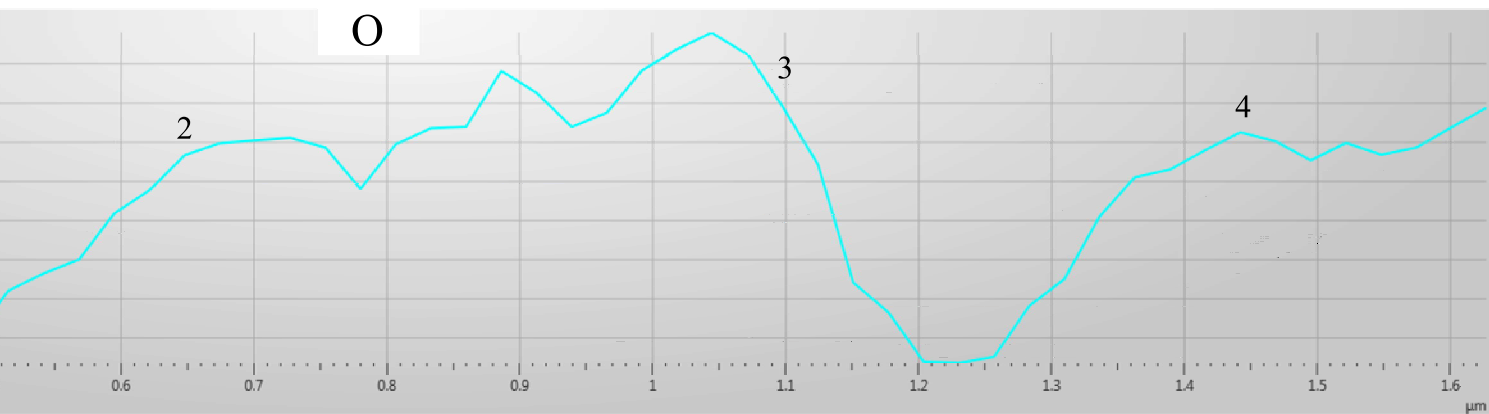
*Accepted Manuscripts* are published online shortly after acceptance, before technical editing, formatting and proof reading. Using this free service, authors can make their results available to the community, in citable form, before we publish the edited article. We will replace this *Accepted Manuscript* with the edited and formatted *Advance Article* as soon as it is available.

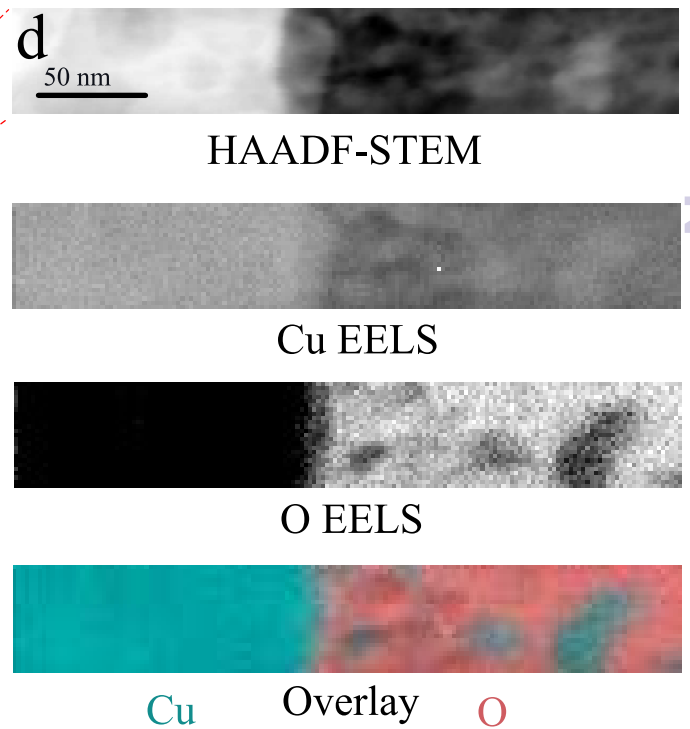
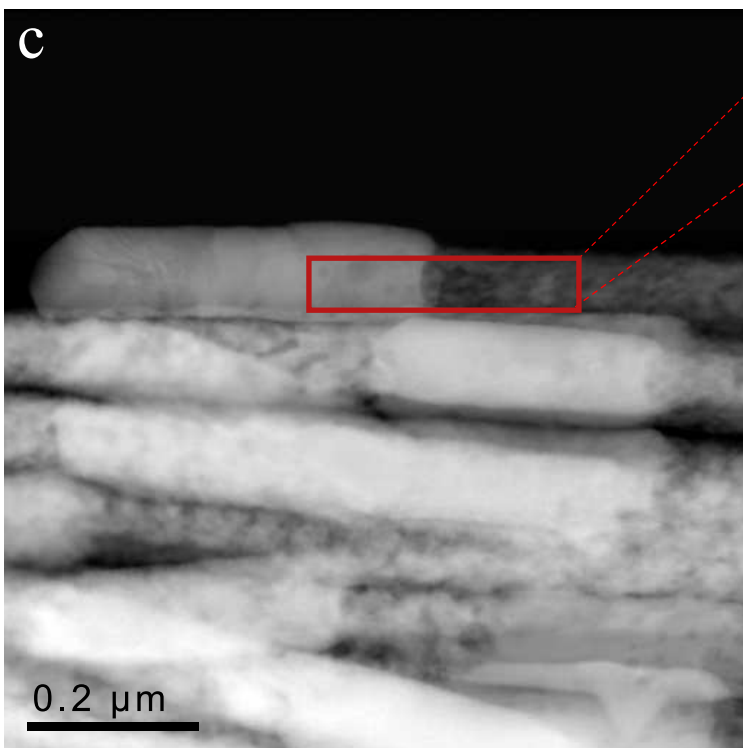
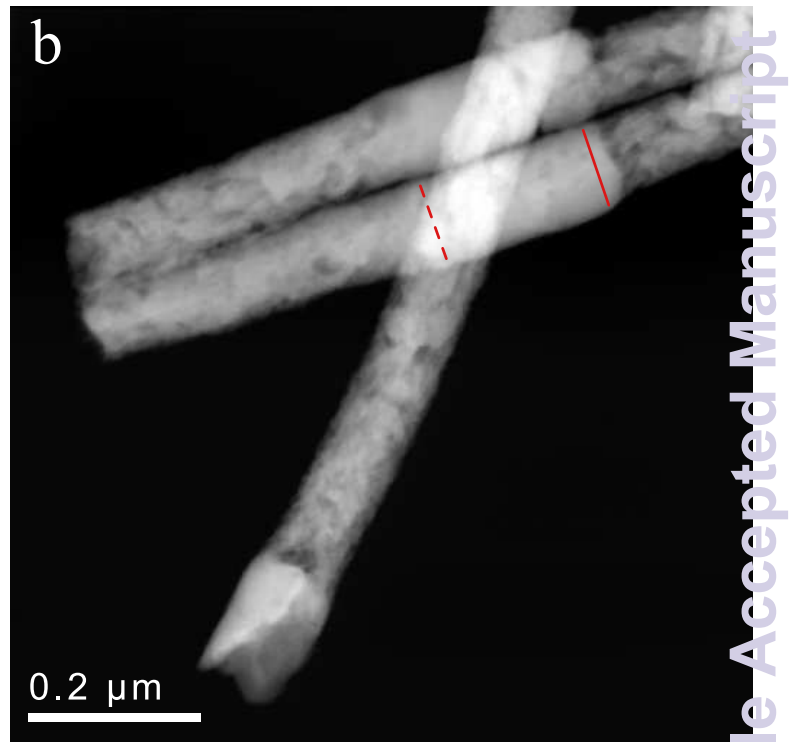
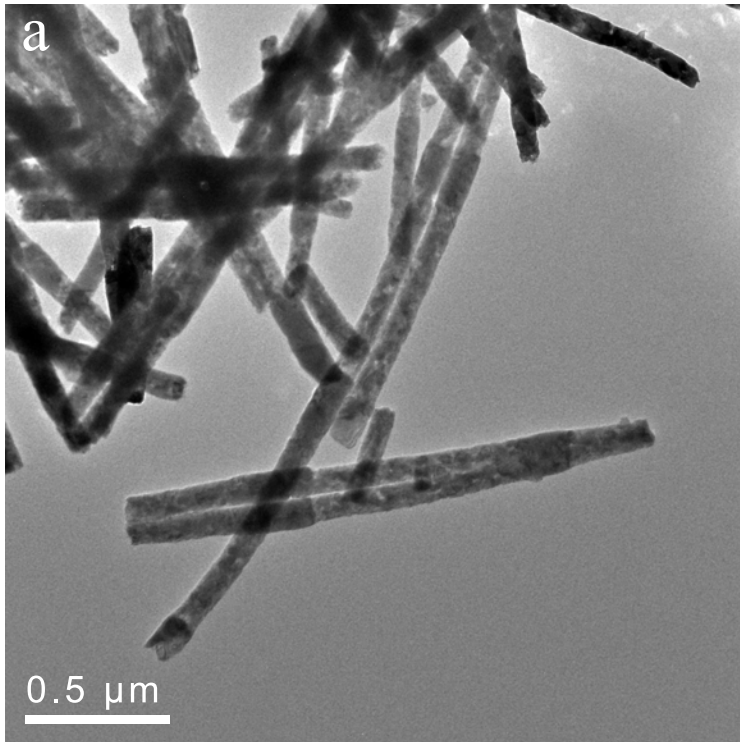
You can find more information about *Accepted Manuscripts* in the [Information for Authors](#).

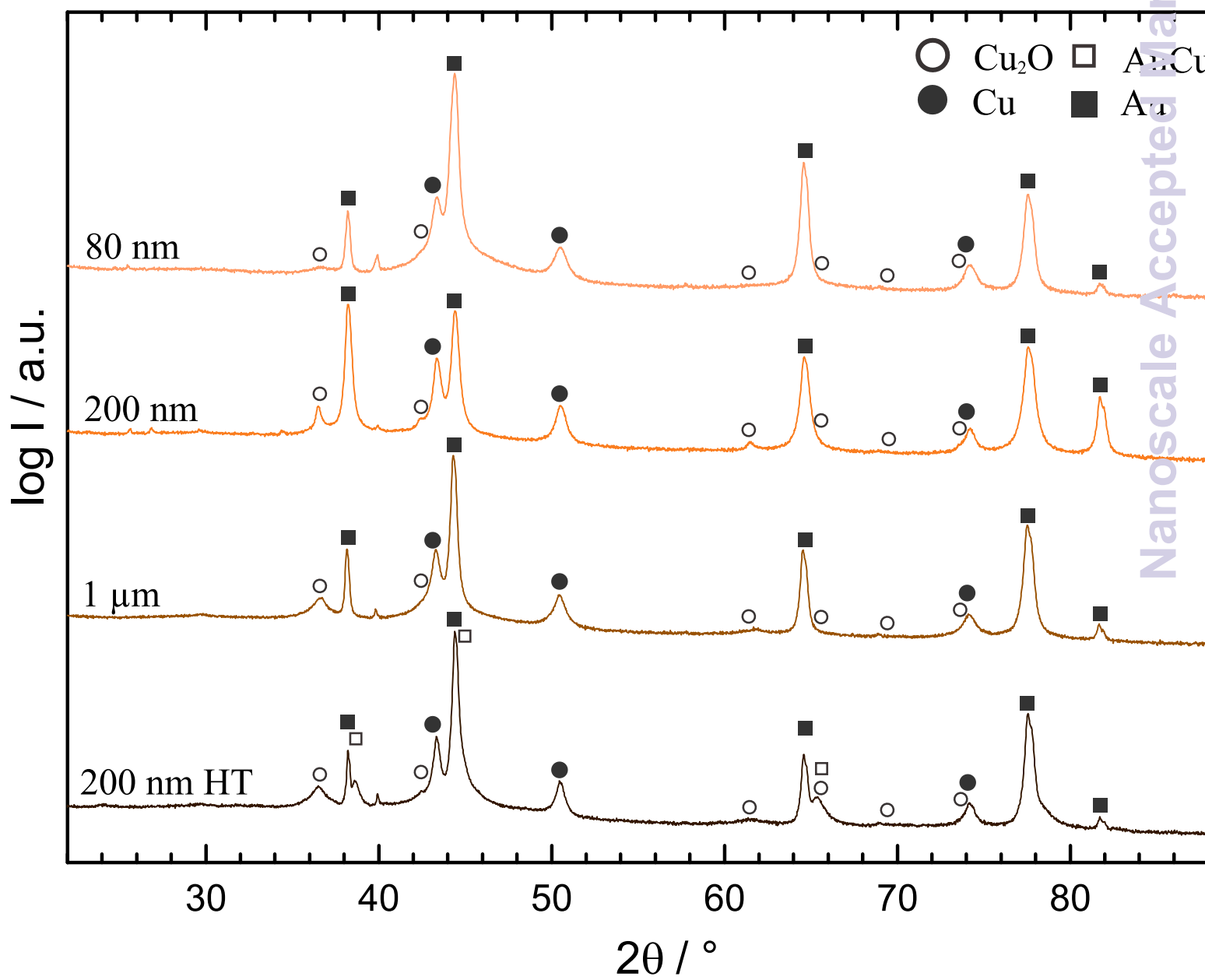
Please note that technical editing may introduce minor changes to the text and/or graphics, which may alter content. The journal's standard [Terms & Conditions](#) and the [Ethical guidelines](#) still apply. In no event shall the Royal Society of Chemistry be held responsible for any errors or omissions in this *Accepted Manuscript* or any consequences arising from the use of any information it contains.

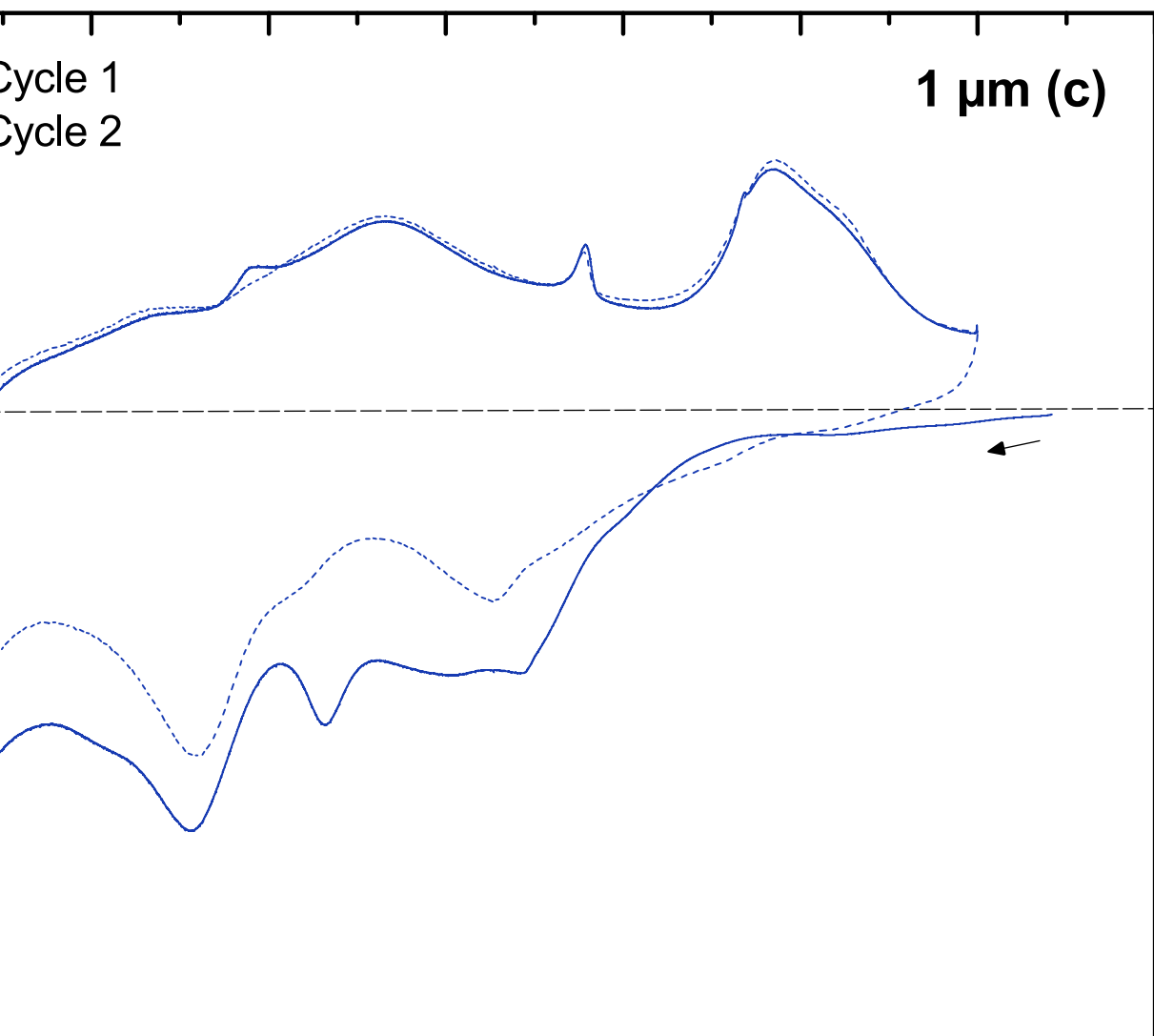
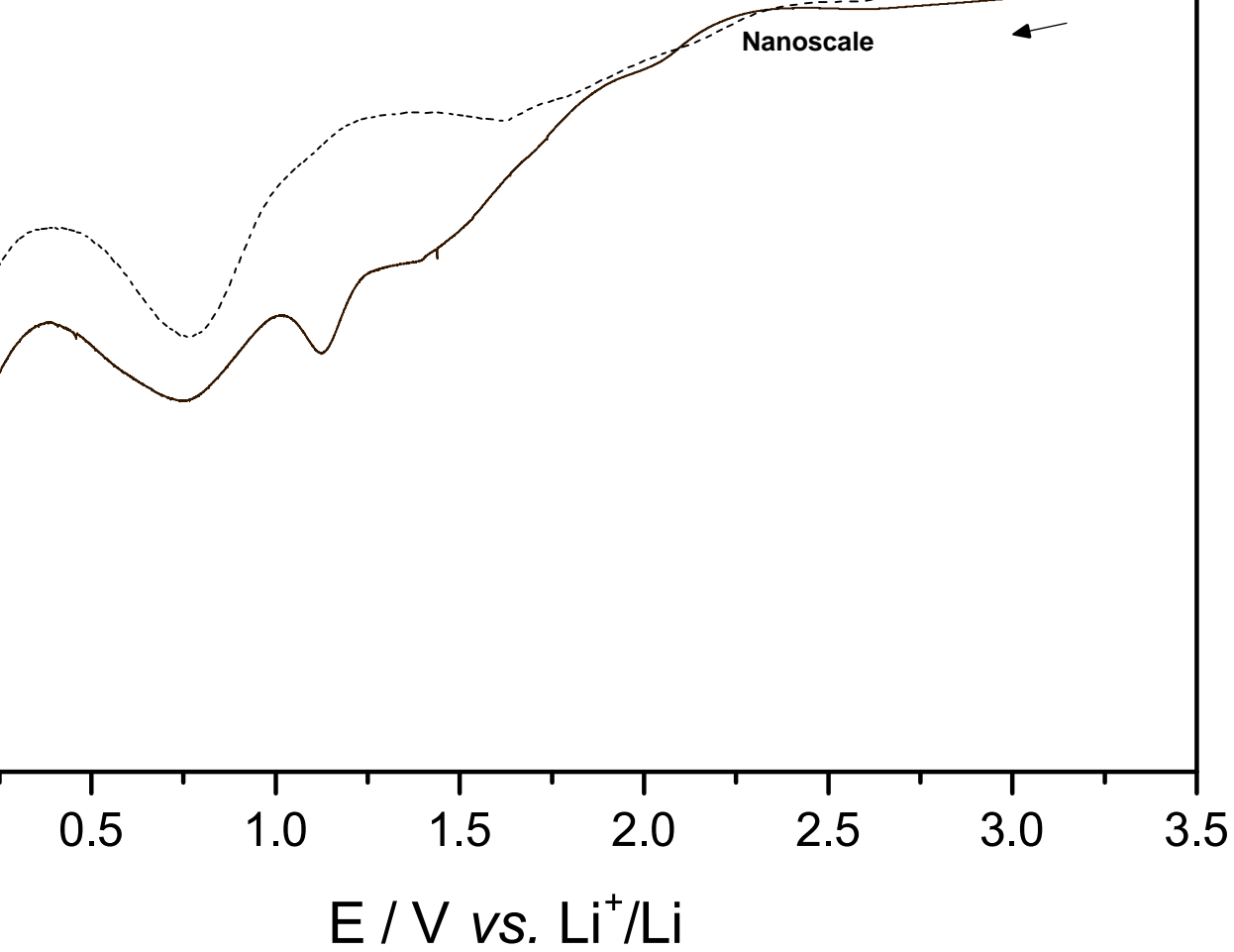


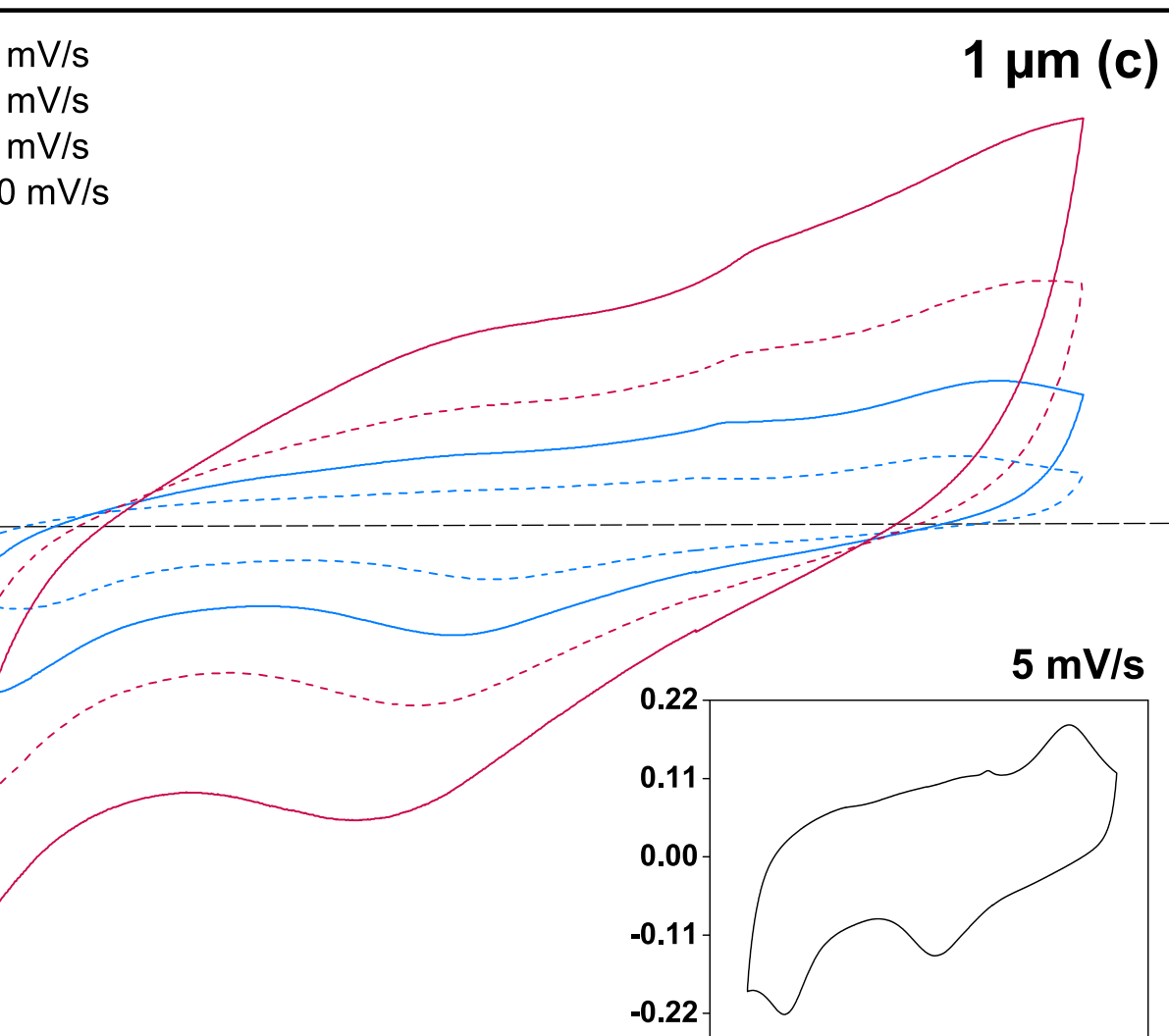
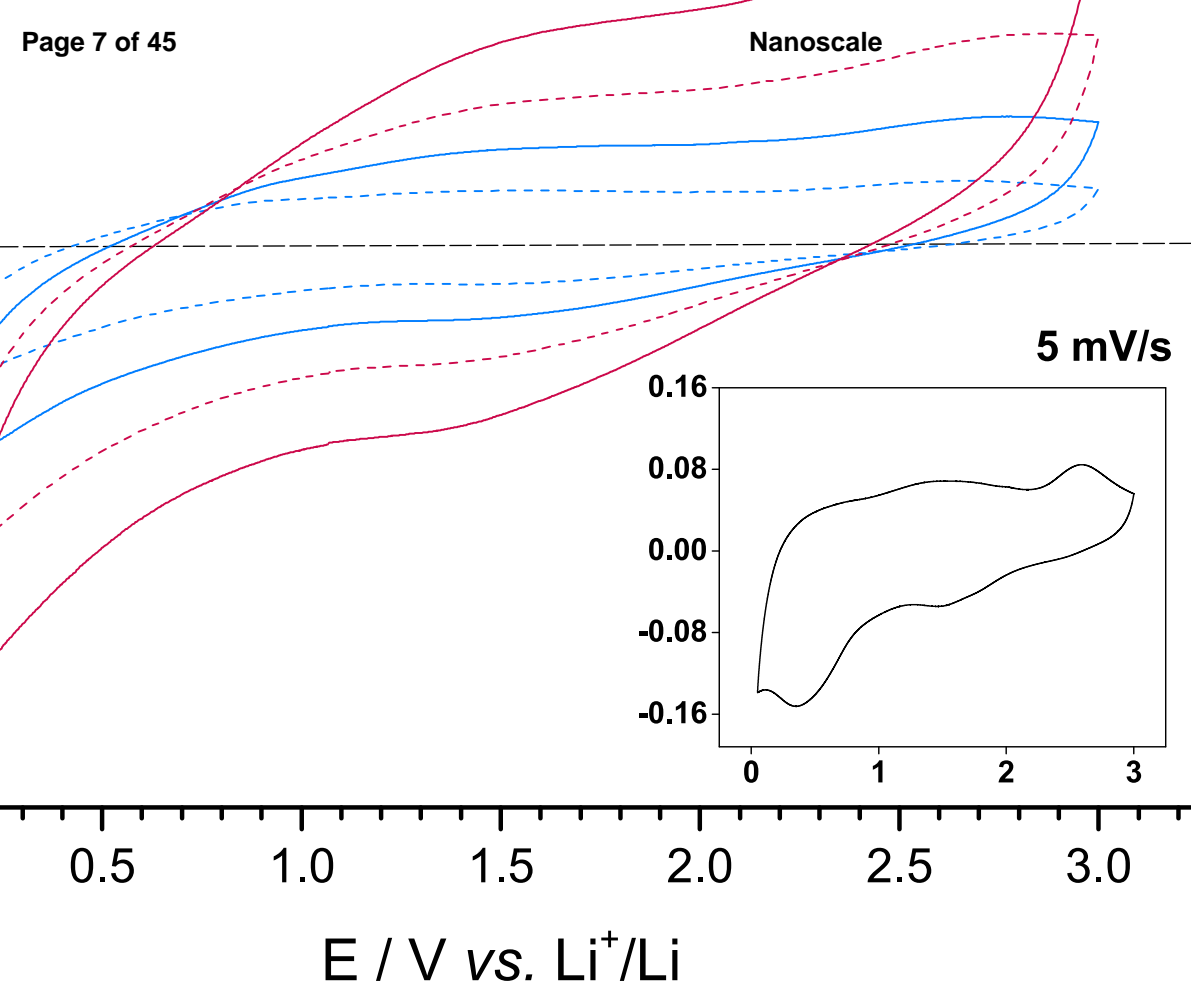


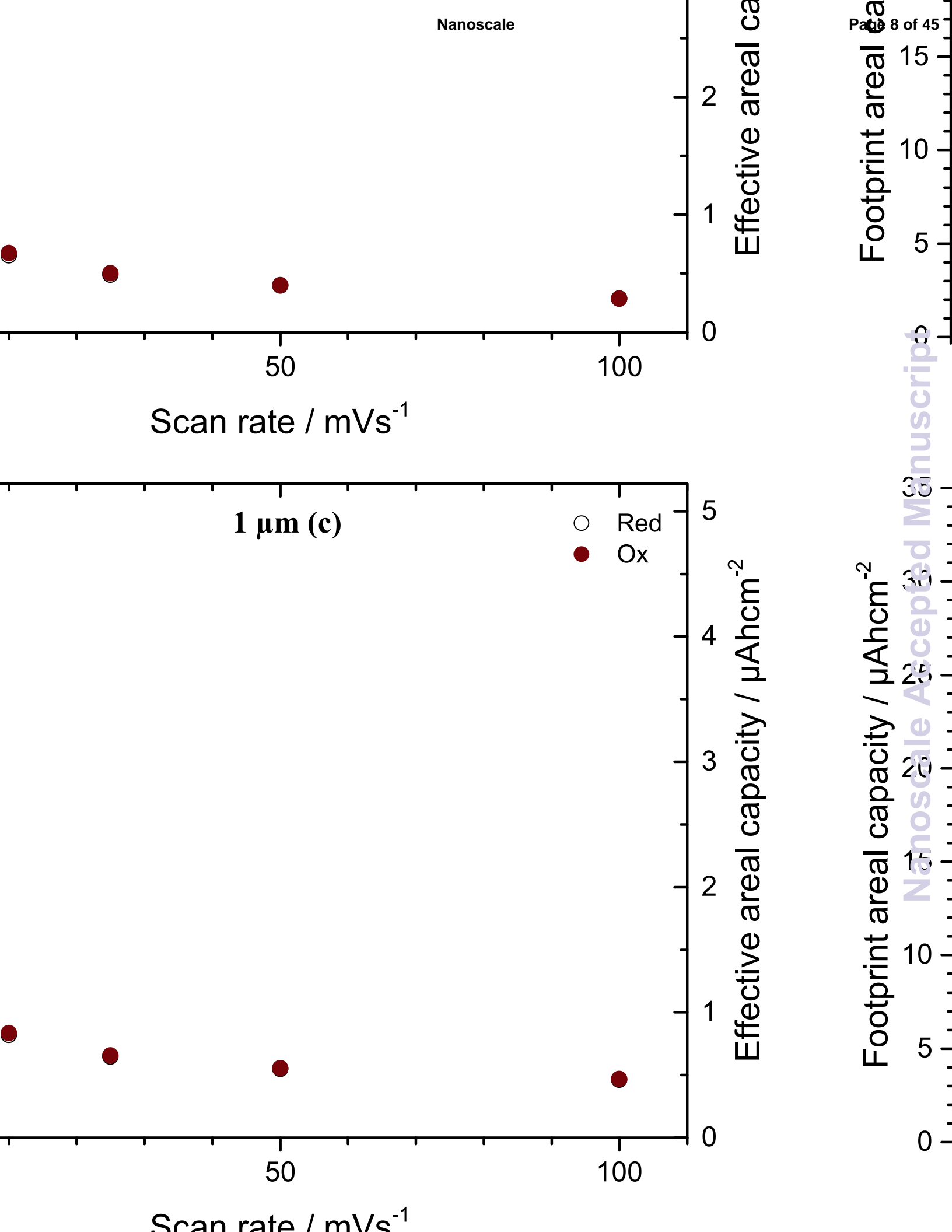


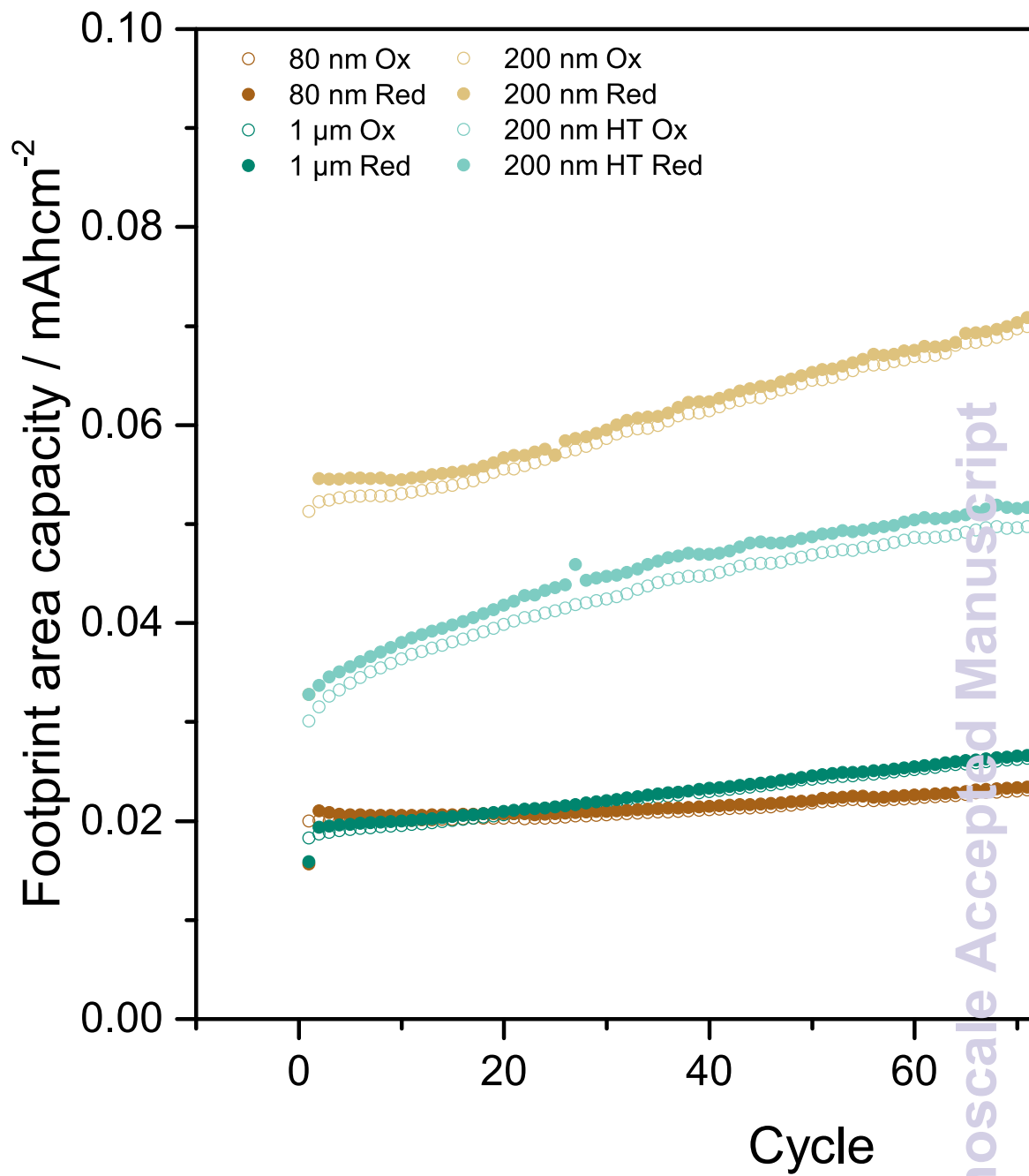




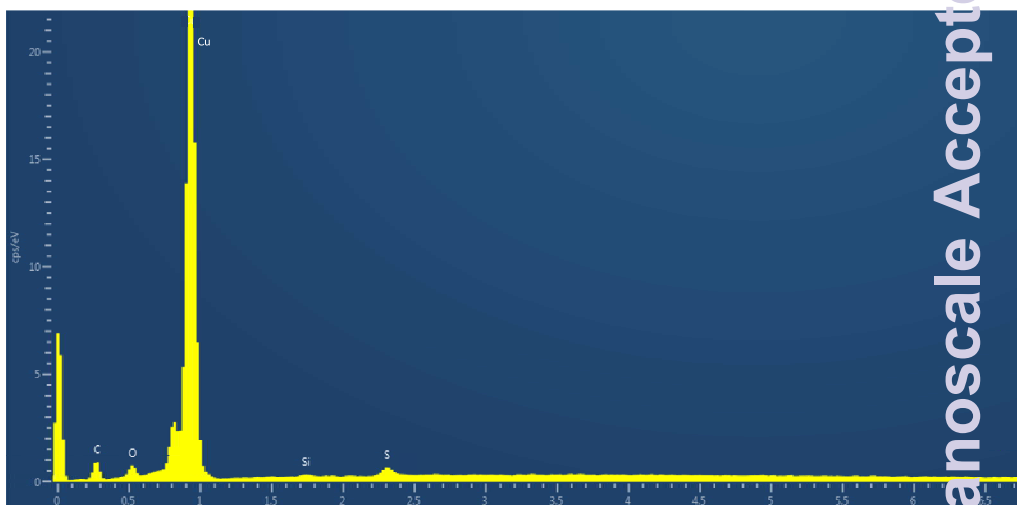
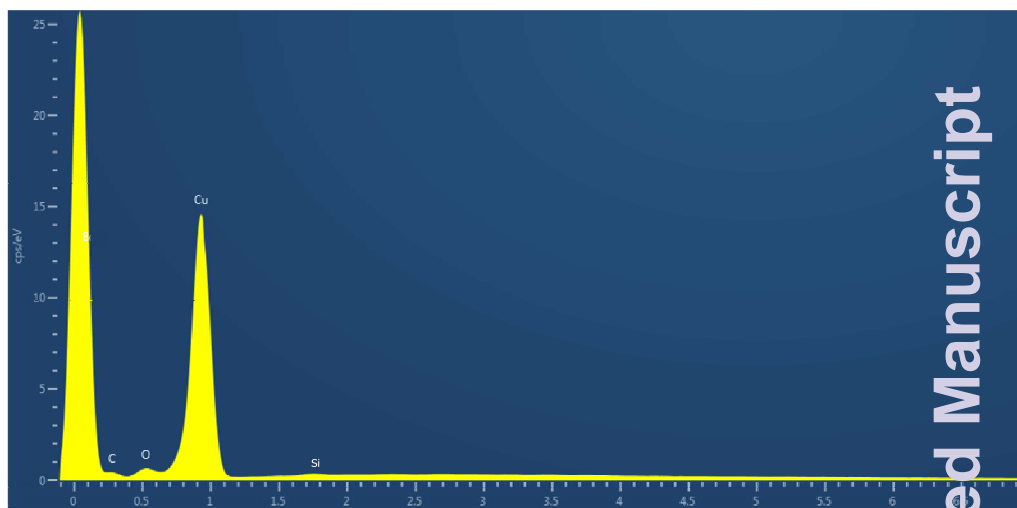
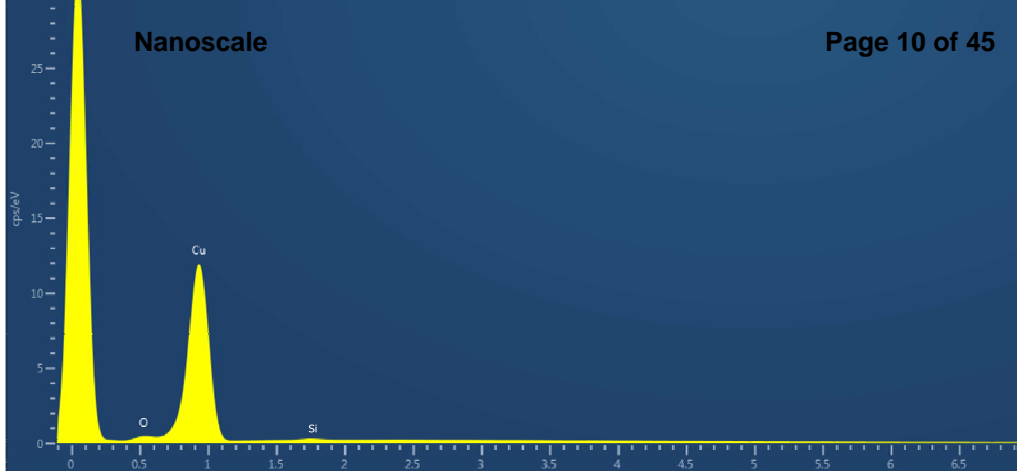


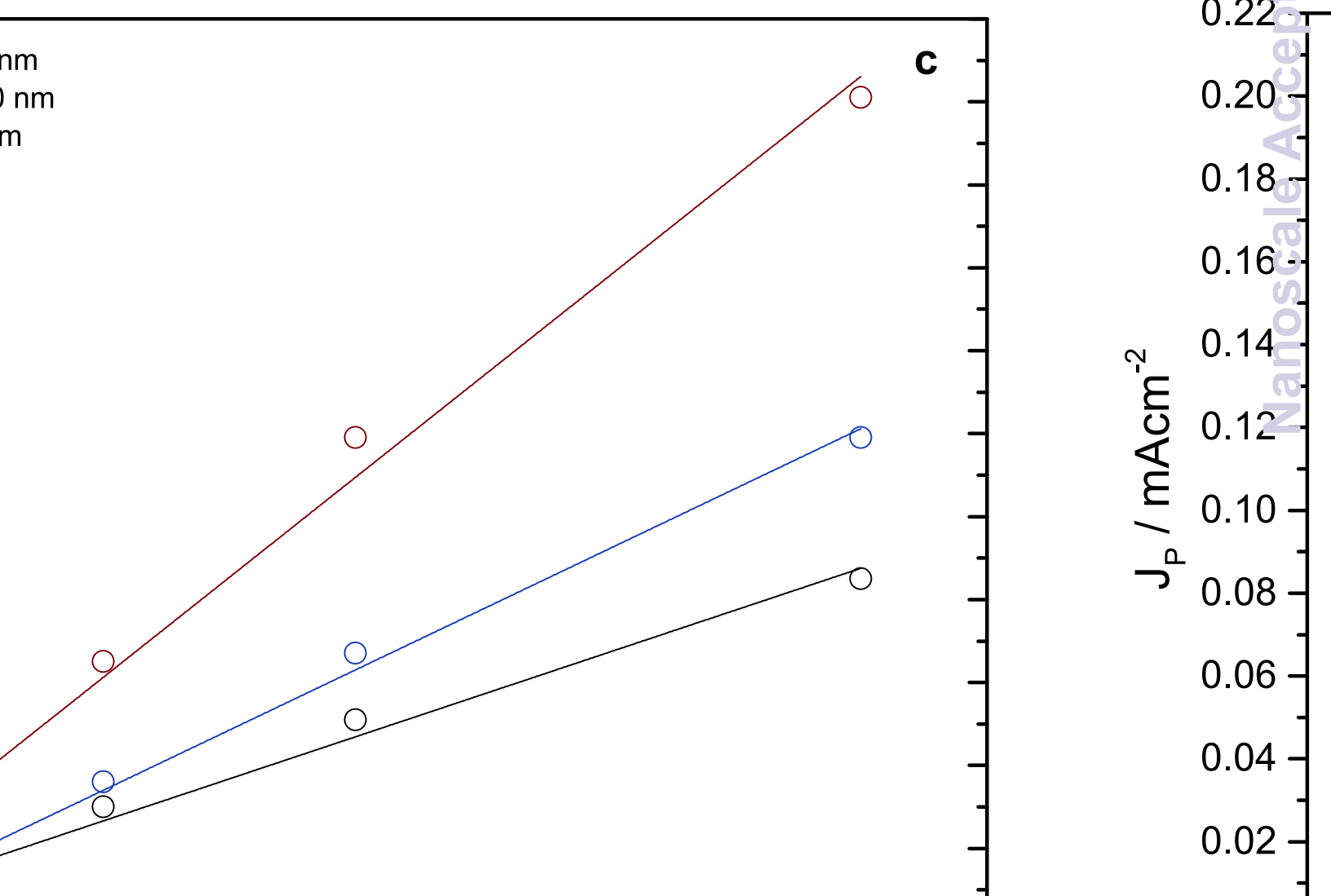
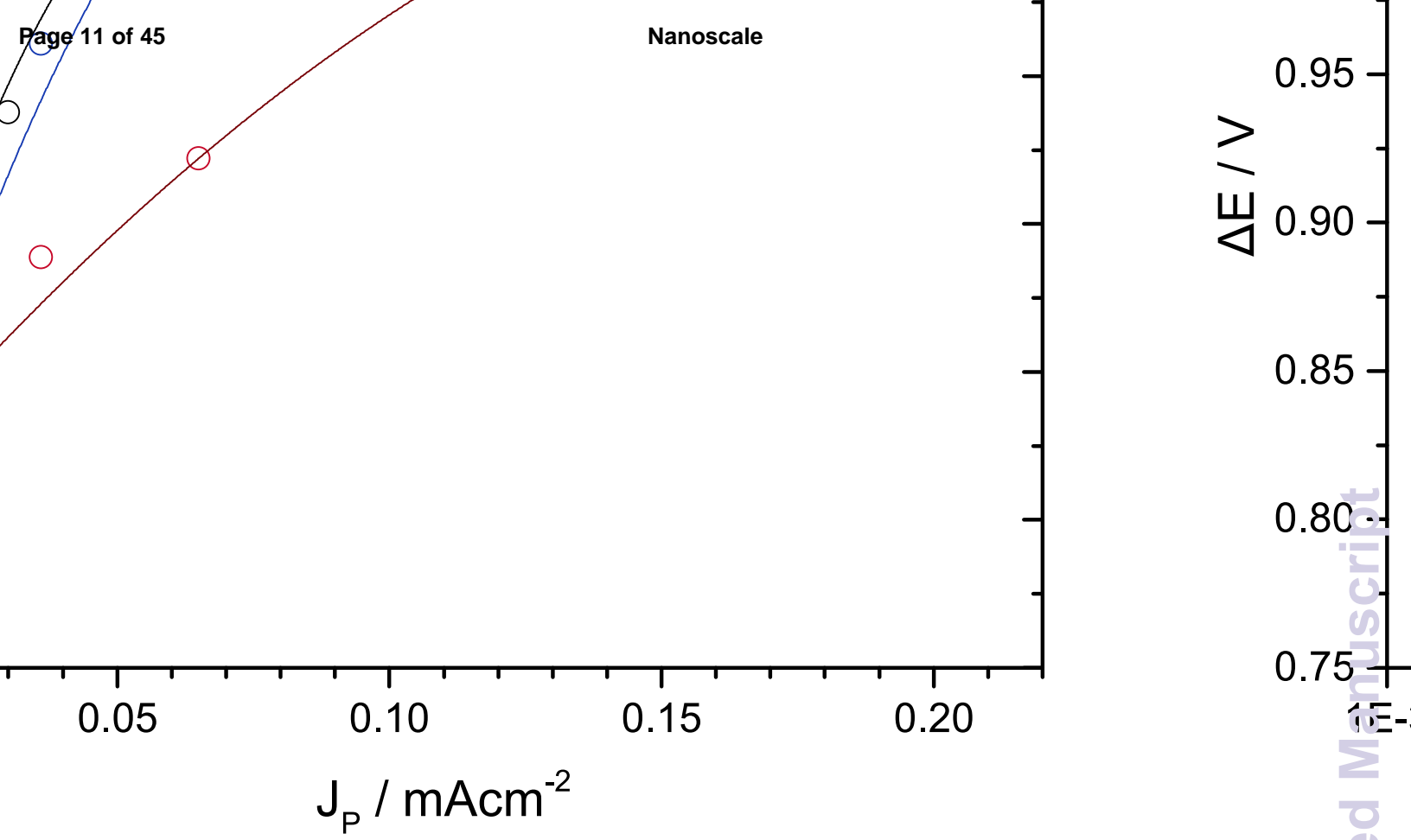




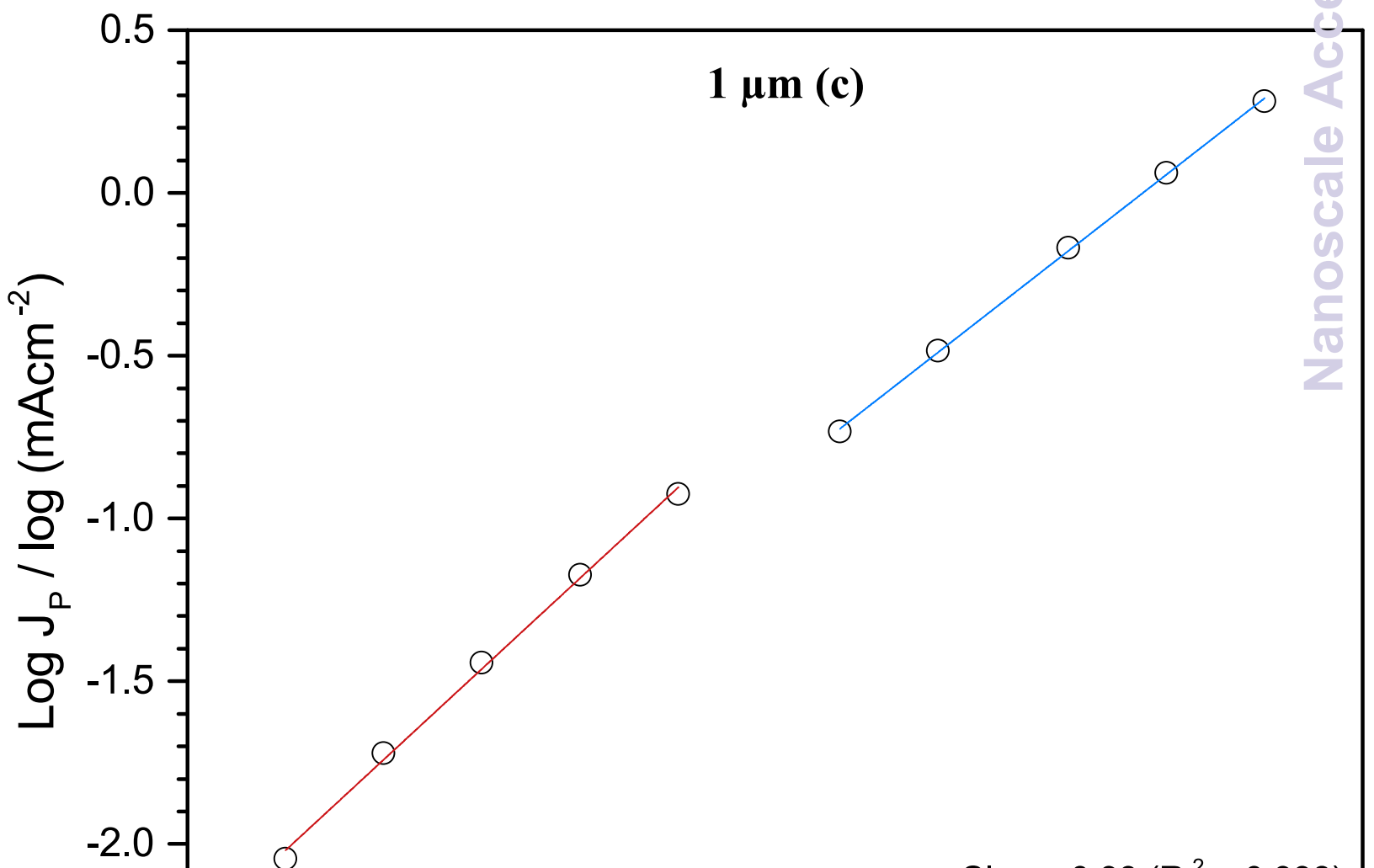
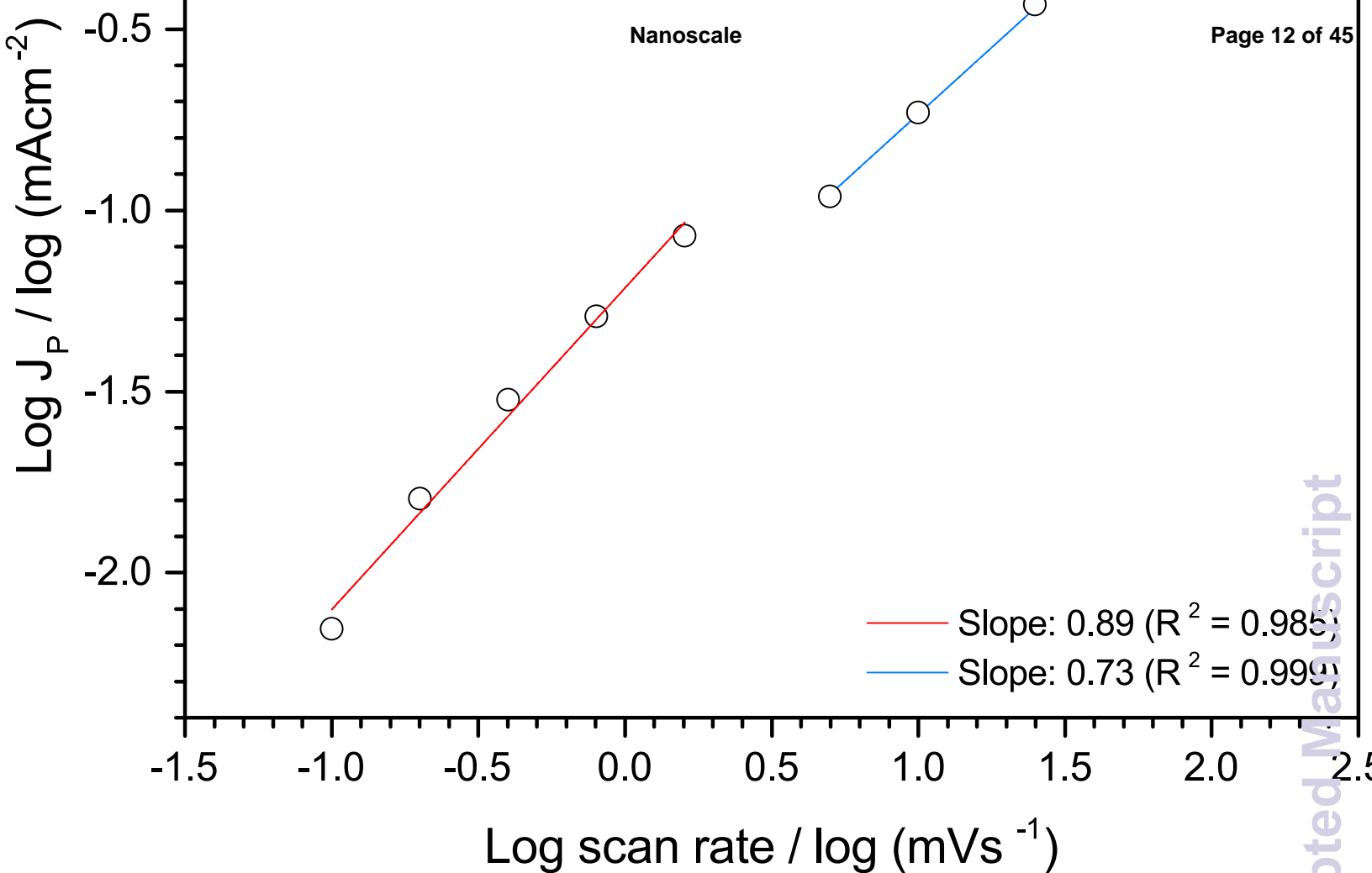


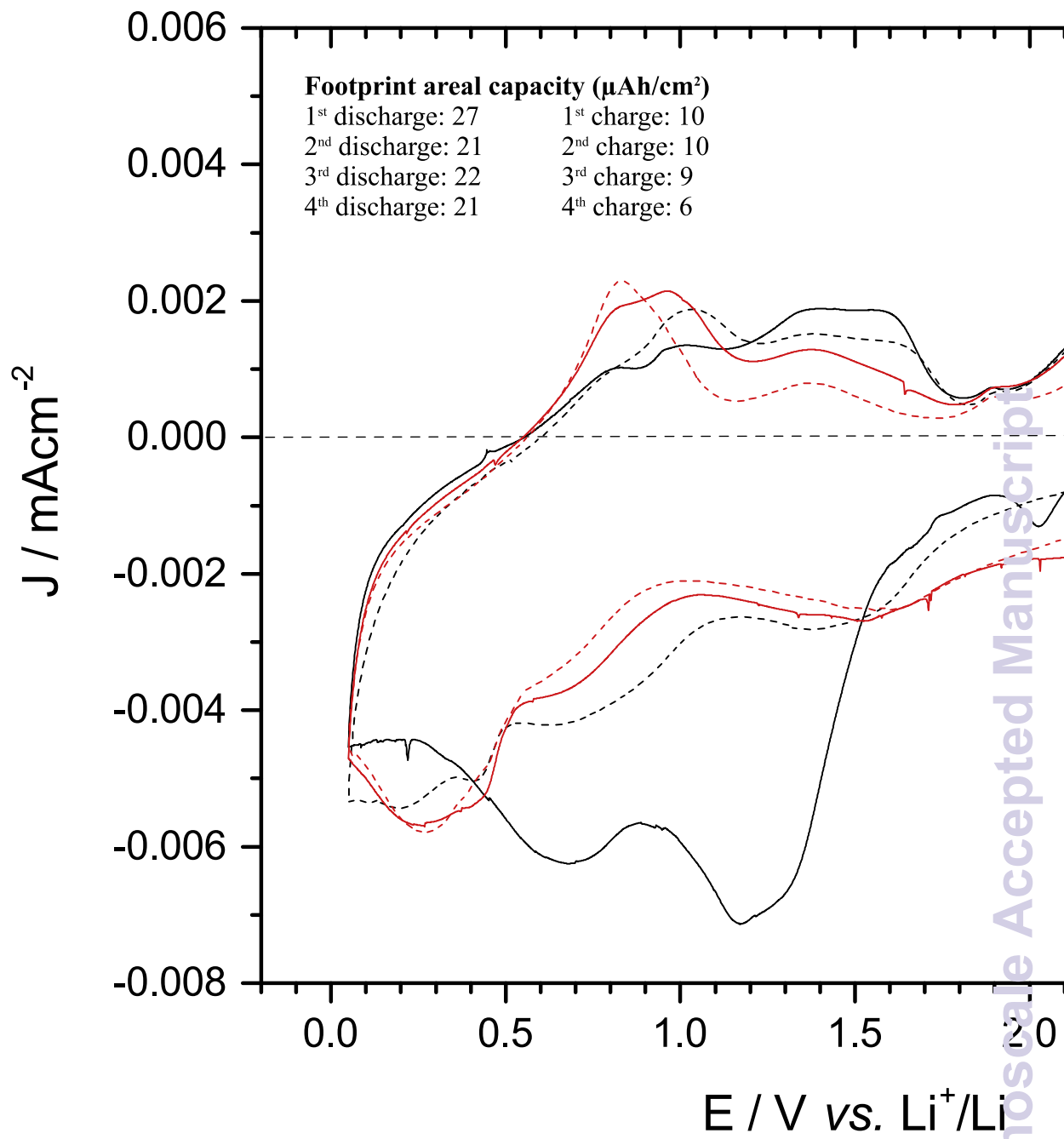
Nanoscale Accepted Manuscript





Nanoscale Accepted Manuscript





## Electrochemical fabrication and characterization of Cu/Cu<sub>2</sub>O multi-layered micro and nanorods in Li-ion batteries

David Rehnlund<sup>1</sup>, Mario Valvo<sup>1</sup>, Cheuk-Wai Tai<sup>2</sup>, Jonas Ångström<sup>1</sup>, Martin Sahlberg<sup>1</sup>,  
Kristina Edström<sup>1</sup>, Leif Nyholm<sup>1</sup>

<sup>1</sup>*Department of Chemistry – Ångström Laboratory, Uppsala University*

*Box 538 75121, Uppsala, Sweden.*

<sup>2</sup>*Department of Materials and Environmental Chemistry, Arrhenius Laboratory, Stockholm University, 106 91, Stockholm, Sweden.*

Corresponding author: [leif.nyholm@kemi.uu.se](mailto:leif.nyholm@kemi.uu.se)

Tel: +46 (0)18 4713742, fax: +46 (0)18 513548

**Keywords:** Electrodeposition, Cuprous oxide, Multilayers, 3-D electrodes, Conversion reactions

### *Abstract*

Electrodes composed of freestanding nano- and microrods composed of stacked layers of copper and cuprous oxide have been fabricated using a straightforward one-step template-assisted pulsed galvanostatic electrodeposition approach. The approach provided precise control of the thickness of each individual layer of the high-aspect-ratio rods as was verified by SEM, EDS, XRD, TEM and EELS measurements. Rods with diameters of 80, 200 and 1000 nm were deposited and the influence of the template pore size on the structure and

electrochemical performance of the conversion reaction based electrodes in lithium-ion batteries was investigated. The multi-layered  $\text{Cu}_2\text{O}/\text{Cu}$  nano- and microrod electrodes exhibited a potential window of more than 2 V, which was ascribed to the presence of a distribution of  $\text{Cu}_2\text{O}$  (and Cu, respectively) nanoparticles with different sizes and redox potentials. As approximately the same areal capacity was obtained independent of the diameter of the multi-layered rods the results demonstrate the presence of an electroactive  $\text{Cu}_2\text{O}$  layer with a thickness defined by the time domain of the measurements. It is also demonstrated that while the areal capacity of the electrodes decreased dramatically when the scan rate was increased from 0.1 to 2  $\text{mV s}^{-1}$ , the capacity remained practically constant when the scan rate was further increased to 100  $\text{mV s}^{-1}$ . This behaviour can be explained by assuming that the capacity is limited by the lithium ion diffusion rate through the  $\text{Cu}_2\text{O}$  layer generated during the oxidation step. The electrochemical performance of present type of 3-D multi-layered rods provides new insights into the lithiation and delithiation reactions taking place for conversion reaction materials such as  $\text{Cu}_2\text{O}$ .

### *1. Introduction*

There is currently a large interest in nanolayered materials mainly as a result of the early fundamental research on superlattice structured materials in the late 1980s<sup>1</sup> which propelled the development of nanoscaled compositionally modulated coatings. The possibility of engineering multi-layered nanostructures with a wide variety of compositions has since then attracted a great deal of scientific interest. Superlattice structures, especially nanostructures, have been found to exhibit interesting properties with respect to a wide range of applications<sup>2-6</sup>. Superlattice nanostructures with modified energy band-gap have thus found to be promising for solar conversion<sup>5, 6</sup> while the giant magnetoresistance effect of magnetic

superlattice structures is highly attractive to the semiconductor industry<sup>2-4</sup>. Tribologically advantageous properties have likewise been demonstrated for CrN/NbN superlattice thin films<sup>7, 8</sup>. At present, vacuum deposition methods such as sputtering and molecular beam epitaxy (MBE) are generally employed for the manufacturing of periodic superlattices<sup>9-11</sup>. Recent advances in electrodeposition have, however, enabled well-controlled manufacturing of multilayered films<sup>4, 12-14</sup>, which has paved the way for important developments within this technologically important area.

Electrodeposition constitutes a particularly promising tool for inexpensive manufacturing of nanostructured electrodes (which are attractive for e.g. energy storage applications<sup>15</sup>) as the morphology, thickness and aspect-ratio of the deposits can be precisely controlled by adjusting the deposition parameters. Electrodeposition can also be used for the deposition of metal oxides<sup>16-18</sup> either via precipitation of metal oxides as a result of an electrochemically increased local pH, or by oxidation of a previously deposited metal layer. Electrochemical co-deposition of alloys and mixtures of oxides have likewise been described<sup>13, 16-18</sup> and superlattice thin films can likewise be deposited using electrochemical atomic layer deposition<sup>19, 20</sup>. Despite the progress within the field of electrodeposition, relatively little attention has so far been paid to electrodeposition of multilayers composed of stacked metal - metal oxide layers<sup>13, 16, 17</sup>. The latter is most likely due to the fact that such depositions are fundamentally difficult since the metal oxide layers should be reduced during the deposition of the metal layers while the metal layers should be oxidized during the deposition of the oxide layers. Deposition of metal and metal oxide multilayer structures can, nevertheless, be realized if the metal layers become passivated by the formation of an oxide layer<sup>21</sup> (preventing a complete oxidation of the metal layer) or when metal layers are formed on top of the metal oxide layers<sup>13, 22</sup>. While anodic passivation of metals is a well-known phenomenon<sup>21, 23</sup>, cathodic passivation of oxide layers has so far received much less

attention, although the effect has been described by Eskhult et al.<sup>13, 22</sup> in connection with the deposition of Cu/Cu<sub>2</sub>O multilayer structures on planar substrates.

Multi-layered nanostructures of Cu/Cu<sub>2</sub>O have been proposed for solar conversion applications such as water splitting based on the beneficial optical properties of cuprous oxide<sup>24, 25</sup>. Copper and cuprous oxide based nanostructures are likewise interesting for use in energy-storage applications such as Li-ion batteries since Cu<sub>2</sub>O can serve as an anode material via a conversion reaction mechanism while copper can be used as a current collector<sup>26, 27</sup>. In the latter case the nanostructured electrodes can provide significantly increased areal capacities (as well as areal energy and power densities)<sup>28, 29</sup>. Multi-layered Cu/Cu<sub>2</sub>O nanostructures could therefore provide new exciting possibilities with respect to energy production and storage.

As has been demonstrated by several research groups, mixed layers or multilayer structures of Cu and Cu<sub>2</sub>O can be obtained using both galvanostatic and potentiostatic electrodepositions<sup>13, 22, 30-34 35-37</sup>. Layered nanostructures of copper/cuprous oxide can thus be deposited from alkaline copper (II) solutions containing suitable ligands by employing constant current conditions giving rise to spontaneous potential oscillations<sup>13, 35, 36</sup>. Based on the latter effect, which was found to be due to local variations in the pH at the electrode surface<sup>13</sup>, it is, unfortunately, difficult to make distinct Cu<sub>2</sub>O layers with a thickness of more than about 10 nm. Eskhult and Nyholm<sup>22</sup> have, on the other hand, shown that multilayer structures containing Cu and Cu<sub>2</sub>O layers, with individually controllable thicknesses of up to about 100 nm, can be deposited using a pulsed galvanostatic deposition approach, while Fujita et al.<sup>38</sup> demonstrated potentiostatic deposition of a Cu<sub>2</sub>O/Cu/Cu<sub>2</sub>O structure with layer thicknesses of 40, 30 and 40 nm, respectively. It has further been shown<sup>22</sup> that the deposition of Cu on Cu<sub>2</sub>O is the critical step in the fabrication of the latter multilayers and that cuprous oxide layers, formed by comproportionation and precipitation from the solution, facilitate the

copper deposition process<sup>22</sup>. Although Leopold *et al.*<sup>30</sup> have demonstrated electrodeposition of microrods composed of intermixed copper and cuprous oxide there are to the best of our knowledge no reports of the electrodeposition of freestanding micro or nanorods composed of stacked multilayers of Cu and Cu<sub>2</sub>O.

The aim of the present work is to demonstrate electrodeposition of micro and nanorods composed of multilayers of copper and cuprous oxide with different diameters and layer thicknesses. It is shown that such multi-layered rods can be deposited using a one-step electrochemical synthesis approach involving pulsed galvanostatic template-assisted electrodeposition. Rods with three different diameters displaying different Cu and Cu<sub>2</sub>O layer thicknesses, all of which were characterized by SEM, EDS, XRD, TEM, EELS and cyclic voltammetry using Li-ion battery cells, are demonstrated and the effect of the rod diameter and layer thickness on the electrochemical performance of the Cu<sub>2</sub>O conversion reaction based Li-ion battery electrode material is discussed. It is demonstrated that the present deposition approach provides new and exciting possibilities for the manufacturing of multi-layered nanostructures suitable for use in energy production and storage applications and that the Li-ion battery characterization provides new insights into the electrochemical reactions taking place within conversion reactions materials such as Cu<sub>2</sub>O.

## 2. Experimental

### 2.1 Growth of multi-layered Cu/Cu<sub>2</sub>O rods

The electrodeposition of the multi-layered micro and nanorods was carried out based on the combination of a previously described pulsed galvanostatic approach<sup>22</sup> and a template based approach<sup>29</sup> developed for the electrodeposition of copper micro and nanorod electrodes for Li-ion microbatteries. The multi-layered Cu/Cu<sub>2</sub>O nanorods were consequently grown on copper substrates (Cu foil 99.9%, Goodfellow) via template-assisted electrodeposition from an electrolyte containing 0.4 M copper sulphate (CuSO<sub>4</sub>·5H<sub>2</sub>O, Merck) and 1.6 M sodium citrate (HOC(COONa)(CH<sub>2</sub>COONa)<sub>2</sub>·2H<sub>2</sub>O, Sigma Aldrich) with a pH adjusted to pH 10.9. The copper substrates were first ultra-sonicated in ethanol for 15 minutes and then rapidly cleaned in 1.0 M H<sub>2</sub>SO<sub>4</sub>. Copper rods with diameters of about 1 μm, 200 nm and 80 nm diameters were electrodeposited using polycarbonate (PC) membranes (Cyclepore, Whatman) with reported aperiodic pore diameters of 1 μm, 200 nm and 50 nm, respectively.

The electrochemical cell utilized in the electrodeposition process was composed of the copper substrate, an electrolyte soaked polycarbonate membrane, an electrolyte soaked glass fibre separator and a copper foil used as counter electrode, all positioned between two plastic plates equipped with copper foil contacts in the mentioned order. The entire assembly was then compressed and placed vertically in a beaker containing the electrolyte solution and a copper foil serving as the reference electrode. All electrodeposition potentials are given with respect to the potential of the copper foil reference electrode (which was found to be -0.22 V vs. Ag/AgCl (sat'd) for the utilized electrolyte).

The multi-layered nanorods were electrodeposited at 50 °C using a pulsed galvanostatic procedure utilizing a Versastat potentiostat/galvanostat. Each cuprous oxide layer was deposited employing a pulsed scheme composed of 700 cycles each involving i) a cathodic

current pulse of  $1 \text{ mAcm}^{-2}$  for 0.1 s and ii) a cathodic current pulse of  $0.1 \text{ mAcm}^{-2}$  for 1 s. The copper layers were, on the other hand, electrodeposited using a cathodic current of  $10 \text{ mAcm}^{-2}$  with a duration of 55 seconds. The  $\text{Cu}_2\text{O}$  and Cu deposition procedures were repeated 14 times to yield rods composed of 14 Cu and  $\text{Cu}_2\text{O}$  layers, respectively. After the deposition, the membrane was dissolved in dichloromethane, thus exposing the freestanding rod based electrode.

## 2.2 Structural and chemical characterization

The surface morphology and elemental composition of the multi-layered micro and nanorods were analysed with a Zeiss MERLIN high-resolution scanning electron microscope (HR-SEM) equipped with an energy dispersive X-ray (EDS) detector (Oxford Instruments). The presented micrographs and EDS spectra were collected at an acceleration voltage of 15 kV and both secondary and backscattered electrons were used to obtain the respective images. The contrast generated by the different electron scattering powers associated with the elements and compounds present in the multi-layered rods (i.e. Cu and  $\text{Cu}_2\text{O}$ ) was also analysed with a dedicated in-lens backscattered electron detector (BSED operated at a negative bias potential of 1500 V).

The transmission electron microscopy (TEM) study was carried out with a JEOL JEM-2100F microscope operated at 200 kV and equipped with a Gatan Ultrascan 1000 CCD camera and a post-column energy filter (GIF Tridiem). The nanorods were scratched off from the substrate with a diamond scribe onto a TEM grid with holey carbon supporting films. TEM sample preparation was done in an Ar-filled glove box. A vacuum-transfer holder was used to transfer the TEM grid from glove box to microscope column. High-angle annular dark-field scanning transmission electron microscopy (HAADF-STEM), also known as Z-

contrast imaging, and electron energy loss spectroscopy (EELS) analyses were likewise conducted using the same microscope. The probe size and camera length used were 0.7 nm and 2 cm, respectively. EELS maps for the copper L edge (931 eV) and oxygen K edge (532 eV) were acquired for the nanorods in STEM mode with a spatial drift correction and a sub-pixel scanning modality enabled.

Crystal structural information was obtained with X-ray diffraction (XRD) using a Bruker D8 Advance diffractometer with a  $\text{CuK}_\alpha$  radiation source and a Lynxeye Energy-Dispersive detector. The samples were mounted on a plastic sample holder using wax and the lattice parameters of the identified phases were determined using the UnitCell<sup>39</sup> program. To correct for possible displacement errors, i.e.  $\cos\theta$  dependent error, an uncoated Au substrate was measured with a NIST 640b Si standard ( $a=5.430922\text{\AA}$ ) applied on top of it and the lattice parameter of Au was then refined after correcting for the displacement error using the Si standard. The refined Au lattice parameter ( $a=4.0810(5)$ ) was in turn used to correct for displacement errors in the measurements of the other samples.

Some multi-layered samples comprising rods with a diameter of 200 nm were also heat treated at 250 °C for 12 hours in vacuum in an Argon filled glove-box to investigate layer/element redistribution effects at elevated temperature. These samples, which were deposited both on copper and gold substrates, were studied with XRD and electrochemistry in connection with the studies of the other samples.

### *2.3 Electrochemical performance in Li-ion batteries*

The electrochemical performance of the obtained nanostructured electrodes composed of multi-layered Cu/Cu<sub>2</sub>O rods with different diameters (i.e. 1  $\mu\text{m}$ , 200 nm and 80 nm) were studied in Li-ion cells employing polymer coated aluminium pouch (i.e. “coffee-bag”) cells,

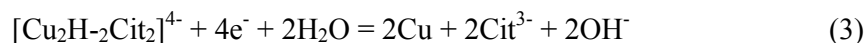
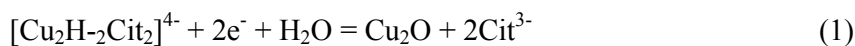
assembled in an Ar-filled M-Braun glove box ( $\text{H}_2\text{O} < 1 \text{ ppm}$ ,  $\text{O}_2 < 1 \text{ ppm}$ ). Prior to assembly, the 3-D electrodes were dried for 5 hours in vacuum at  $120 \text{ }^\circ\text{C}$ . The employed Li-ion cells consisted of a multi-layered 3-D Cu/Cu<sub>2</sub>O sample working electrode and a Li foil counter electrode separated by a Solupore polymer separator soaked with about  $50 \text{ }\mu\text{l}$  of an electrolyte composed of  $1.0 \text{ M LiPF}_6$  dissolved in ethyl carbonate/diethyl carbonate (EC:DEC 2:1). The electrochemical characterization of the cells involved cyclic voltammetry (CV) and chronopotentiometric experiments carried out using a VMP2 Potentiostat/Galvanostat (Bio-Logic). The CV experiments were performed between  $0.05$  and  $3 \text{ V vs. Li}^+/\text{Li}$  using scan rates between  $0.1$  and  $100 \text{ mV s}^{-1}$  while a constant current density of  $30 \text{ }\mu\text{A cm}^{-2}$  and voltage cut-off limits of  $0.05$  and  $3 \text{ V vs. Li}^+/\text{Li}$  were utilized in the chronopotentiometric experiments.

### 3. Results and discussion

#### 3.1 Template-assisted electrodeposition of multi-layered Cu/Cu<sub>2</sub>O nanostructures

As described in the experimental section multi-layered Cu/Cu<sub>2</sub>O nanorods with different diameters were made using template-assisted electrodeposition employing a pulsed galvanostatic technique. The cuprous oxide deposition step involved repeated pulsing of the current density between  $-0.1 \text{ mA cm}^{-2}$  and  $-1 \text{ mA cm}^{-2}$  whereas the copper deposition was carried out using a current density of  $-10 \text{ mA cm}^{-2}$  in analogy with the approach previously used<sup>22</sup> for the deposition on planar substrates. The present approach thus utilises the fact that Cu<sub>2</sub>O is deposited at sufficiently low current densities while deposition of Cu is obtained for higher current densities. As the thicknesses of the individual Cu<sub>2</sub>O and Cu layers merely are determined by the deposition time or the number of deposition pulses employed for each layer the approach could hence be used for the manufacturing of Cu<sub>2</sub>O/Cu multilayer structures with a wide range of layer thicknesses. The Cu<sub>2</sub>O and Cu deposition reactions which can be

described using the following three reactions, have been discussed in detail in our previous publications<sup>13, 22</sup>. In the reactions below the copper ions in the electrolyte are assumed to be present in the form of a predominating copper citrate complex (i.e.  $\text{Cu}_2\text{H}_2\text{Cit}_2^{4-}$ ).



The electrochemical reactions yielding  $\text{Cu}_2\text{O}$  and Cu thus involve Reaction (1) and (3), respectively, and to obtain  $\text{Cu}_2\text{O}$  it is important to use a sufficiently low current density so that Reaction (1) (involving a reduction of Cu(II) to Cu(I)) can support the current. Copper deposition is then obtained by increasing the current density to a value which is compatible with the rate of Reaction (3). As indicated by Reaction (3) the Cu deposition reaction gives rise to an increased local pH at the electrode surface which previously has been shown to produce spontaneous potential oscillations and mixed Cu/ $\text{Cu}_2\text{O}$  deposits during constant current depositions<sup>13, 35, 36</sup>. Since the local pH and the current density determine whether  $\text{Cu}_2\text{O}$  or Cu will be formed<sup>13</sup> it can be difficult to control the thicknesses of the individual layers, particularly when the deposition takes place within narrow pores of a membrane. Note also that Reaction (2) shows that  $\text{Cu}_2\text{O}$  also can be formed by comproportionation whenever a Cu layer is in contact with a solution containing Cu(II) species<sup>13, 29</sup>. The  $\text{Cu}_2\text{O}$ /Cu multilayer deposition is further complicated by the fact that the  $\text{Cu}_2\text{O}$  layer should undergo reduction to Cu during the subsequent Cu deposition step. The completeness of the latter process is, however, limited by the formation of a copper layer on top of the remaining  $\text{Cu}_2\text{O}$  which protects the remaining  $\text{Cu}_2\text{O}$ <sup>13, 22</sup>. This cathodic passivation effect can be compared with the anodic passivation of a metal by the formation of an oxide layer. When template based depositions are carried out concentration gradients will also develop within the pores of the

membrane that further complicate the deposition compared to for depositions on planar substrates.

In the present study, it was found that the problems discussed above could be circumvented using a pulsed galvanostatic approach for three templates with different pore sizes. The deposition chronopotentiograms for the different templates are shown in Figure 1 whereas SEM images of the resulting multi-layered Cu<sub>2</sub>O/Cu rods are depicted in Figure 2. As can be seen in Figure 1, the Cu<sub>2</sub>O layer deposition process comprised a large number (i.e. 700) of short (i.e. 0.1 and 1 s) galvanostatic subpulses with current densities of 1.0 and 0.1 mA cm<sup>-2</sup>, respectively, while the subsequent copper deposition was made using a single 55 s long pulse involving a current density of 10 mA cm<sup>-2</sup>. This procedure was used to ensure that only Cu<sub>2</sub>O was deposited during the Cu<sub>2</sub>O deposition pulses and that the length of the Cu pulse was maintained short enough not to give rise to spontaneous potential oscillation effects. Depositions of planar multilayers have shown a typical onset time for the spontaneous oscillations of about 60 s for the Cu deposition pulse<sup>13 22</sup>. As is seen in Figure 1, the initial Cu<sub>2</sub>O and Cu depositions took place at about 0.15 and -0.27 V vs. Cu<sup>2+</sup>/Cu for the 50 nm template while more negative potentials were obtained for the 200 nm and 1 μm templates. The latter can most likely be explained by a lower overpotential (due to a lower current density in each pore) for the 50 nm template which had a higher pore density than the other two templates (see Table S2 in the Supporting Information). The negative shift in the deposition potentials as a function of the deposition time seen for all templates can either be ascribed to an increased iR drop as a result of the growing Cu<sub>2</sub>O containing rods or a change in the concentration of the electroactive copper complex. The latter is, however, less likely given the high Cu(II) concentration (i.e. 0.4 M) in the electrolyte. For the 1 μm template (and also for the 200 nm template at times longer than about 6000 s) it can also be seen that the Cu<sub>2</sub>O deposition potential became more and more positive for each Cu<sub>2</sub>O deposition substep

while the  $\text{Cu}_2\text{O}$  deposition potential remained approximately constant during each  $\text{Cu}_2\text{O}$  deposition substep for the 50 nm template. This effect could be explained by the previously discussed<sup>13 22</sup> problems associated with the initial deposition of  $\text{Cu}_2\text{O}$  on Cu and the differences in the current density within the pores of the different templates. The results consequently suggest that while Cu deposition also occurred during the initial part of the  $\text{Cu}_2\text{O}$  deposition step for the 1  $\mu\text{m}$  template, the current density within the pores was low enough to yield mainly  $\text{Cu}_2\text{O}$  deposition for the 50 nm template. These data clearly show that it is possible to electrodeposit micro and nanorods composed of multilayers of Cu and  $\text{Cu}_2\text{O}$  using a template approach and that the deposition of well-controlled layers requires very good control of the current densities in the pores of the template.

### *3.2 Microstructure of the Cu/ $\text{Cu}_2\text{O}$ multi-layered rods*

The SEM micrographs depicting the  $\text{Cu}_2\text{O}/\text{Cu}$  multilayer rods seen in Figure 2 clearly show that the rods obtained with the 200 nm and 1  $\mu\text{m}$  templates contained a series of different layers. A closer examination (see below) indicated that the 200 nm rods had a length of approximately 5  $\mu\text{m}$  and Cu and  $\text{Cu}_2\text{O}$  layer thicknesses of 200 nm and 300 nm, respectively, while the 1  $\mu\text{m}$  rods were composed of approximately 350 nm thick Cu layers and 500 nm thick  $\text{Cu}_2\text{O}$  layers yielding a total rod length of about 9  $\mu\text{m}$ . The approximately 3.5  $\mu\text{m}$  long nanorods obtained with the 50 nm template were then found to have a true diameter of about 80 nm (see also the TEM results below) and further analyses showed the presence of Cu and  $\text{Cu}_2\text{O}$  layers with thicknesses of 125 to 250 nm and 400 to 800 nm, respectively (see the TEM results below). These results demonstrate that the thickness of the  $\text{Cu}_2\text{O}$  layers increased as the diameter of the template pores decreased. For the 80 nm rods the average  $\text{Cu}_2\text{O}$  layer was thus 3.2 times thicker than the average Cu layer, as compared to the

Cu<sub>2</sub>O/Cu thickness ratio of 1.4 found for the 1 μm rods. This phenomenon can be explained by the lower current density for the 50 nm template, in good agreement with the chronopotentiometric results discussed above. The present data indicates that the 80 nm, 200 nm and 1 μm rods multi-layered rods contained 79 %, 60 % and 59 % Cu<sub>2</sub>O, respectively.

As is seen in Figures 2b and c, a characteristic ‘bamboo-like’ morphology was found for the 200 nm and 1 μm rods. This effect, which could not be detected by SEM for the 80 nm rods (see Figure 2a), indicated that the diameter of the deposited Cu<sub>2</sub>O and Cu layers differed somewhat. Based on the SEM-EDS data depicted in Figure 3 (which are further discussed below) and TEM data (see below), it is reasonable to assume that the layers with the slightly larger diameter were composed of copper and that the copper layers were coated with an approximately 15 nm thick layer of Cu<sub>2</sub>O, in good agreement with previous findings<sup>29</sup>.

As is described in Figure 3, the composition of each layer of the 1 μm multi-layered rod was analysed using HR-SEM/EDS. EDS spectra (Figure S1 in the Supporting Information) show that all rods were composed of copper and oxygen. The 1 μm sample was also studied using a dedicated backscattered electron detector to reveal the compositional contrast could be obtained for the adjacent phases in the associated images. In Figure 3a the brighter layers correspond to the layers containing a higher density of heavy elements as compared to the darker layers. This indicates that the brighter layers correspond to the Cu layers while the darker layers contain Cu<sub>2</sub>O. To test this hypothesis EDS line scanning was performed along the length of a rod as indicated by the dotted line in Figure 3a. An acceleration voltage of 15 kV was used to access both K-shell and L-shell excited copper electrons and a software specific algorithm was implemented to remove any peak overlap between oxygen and carbon (as the latter features lie in close proximity to each other). In Figure 3b it is seen that a high copper intensity and a low oxygen intensity were found in the regions denoted by 1 and 3 while low copper and high oxygen intensities were found in the regions denoted by 2 and 4.

Even though the oxygen intensities were significantly lower than the copper intensities the variations in the oxygen intensities clearly complement the copper intensities indicating the presence of a  $\text{Cu}_2\text{O}/\text{Cu}$  multi-layered structure. The copper intensity peaks at the points 1 and 3 thus roughly match the oxygen intensity minima located approximately between points 1-2 and 3-4, respectively. The slight shift in the position of the oxygen minima with respect to those of the copper intensity maxima could have been caused by the small angle between the substrate and the EDS detector. This hypothesis is supported by the fact that the distances between the copper intensity maxima and the oxygen intensity minima are approximately the same in Figure 3b.

Since the images obtained with secondary electron detection (SED) contain information solely from secondary electrons, the multilayer effect could have resulted from the presence of layers with the same composition but different surface roughness. This possibility was excluded by using backscattered electron (BSE) imaging (see Figure 3c), where secondary electrons were filtered out and the same region was compared to that imaged by SE. The individual layers seen with the SED were likewise observed with the BSED where the brighter layers represent regions with higher electron densities. As only copper and oxygen are present in the rod, this indicates the presence of layers with different copper concentrations, i.e. layers of Cu and  $\text{Cu}_2\text{O}$ .

To provide a more detailed analysis of the local composition of the Cu/ $\text{Cu}_2\text{O}$  layers and to better evaluate the trend line seen by SEM/EDS, TEM was used to probe the phase boundary where the excitation area can be limited to individual layers. In order to allow electron beam penetration the 80 nm nanorods were imaged as is shown in Figure 4. Low magnification imaging in the bright-field mode (BF) (Figure 4a) confirmed the presence of the multi-layered pattern previously observed by HR-SEM. Contrast variations were also observed across the rods indicating a polycrystalline structure. Differences in crystal

orientation, thickness, length and density were likewise found throughout the rods. These features are demonstrated in Figure 4b where HAADF-STEM imaging with exclusive settings for atomic number contrast was used to probe the phase boundaries between the layers. The red lines enclose a dense region with high contrast, corresponding to a Cu layer, whereas the neighbouring Cu<sub>2</sub>O layers exhibit considerably lower intensities as would be expected since the Cu concentration is lower in Cu<sub>2</sub>O. Upon closer inspection of the interfaces between the Cu and Cu<sub>2</sub>O layers, there seems to be a sharp phase boundary next to the solid red line, as opposed to the dashed red line, which shows a less defined interphase. This observation is interesting, as it suggests that the interphase formed during the deposition of copper differed from that generated during the Cu<sub>2</sub>O deposition. The same trend is in fact also visible in Figure 3d depicting the BSED-SEM image for the 1 μm rod. Based on the chronopotentiograms in Figure 1 it is reasonable to assume that the sharper interface stemmed from copper deposition on Cu<sub>2</sub>O while the deposition of Cu<sub>2</sub>O on copper produced a less well-defined interface. The latter could be explained by the residual copper deposition during the initial part of the Cu<sub>2</sub>O deposition step discussed above.

The interface between two adjacent layers within a 80 nm nanorod was also studied with EELS as is seen in Figure 4c and d. Mapping of the Cu signal revealed a higher Cu concentration in the lighter (i.e. denser) region seen in the HAADF-STEM image (i.e. Figure 4c) while analogous O mapping revealed a well-defined phase boundary with practically no oxygen within the Cu layer. The overlay of both maps shown in Figure 4d, however, clearly shows that Cu nanoparticles were present in the Cu<sub>2</sub>O layer. Although a metal oxide layer should have been present on the Cu surface since the rod had been exposed to air and the Cu(II) containing solution, such a layer could not be detected in the EELS measurements.

As is clearly seen in Figure 4c, the ‘bamboo-like’ morphology observed in the SEM images for the 200 nm and 1 μm rods (see Figure 2) could also be seen for the 80 nm rods

using TEM. It is immediately evident that the diameter of the copper layer was larger than for the  $\text{Cu}_2\text{O}$  layer. One explanation for the ‘bamboo-like’ morphology could then be that the growth of the Cu layers led to a slight expansion of the diameter of the flexible polycarbonate pores. Another possibility is that the Cu layers were coated with a layer of  $\text{Cu}_2\text{O}$  after the removal of the template either due to oxidation by oxygen or comproportionation according to Reaction 2. The latter seems more likely since we have recently used this effect to generate thin  $\text{Cu}_2\text{O}$  coatings on copper nanorods and as the thickness of the  $\text{Cu}_2\text{O}$  layer according to Figure 4c was about 15 nm in good agreement with our previous results<sup>29</sup>.

The SEM and TEM results hence confirm the presence of layers of  $\text{Cu}_2\text{O}$  and Cu within the electrodeposited micro and nanorods and also demonstrate that the ratio between the thicknesses of these layers increased with decreasing current density within the pores of the template.

### *3.3 Phase analyses of the multi-layered nanorods*

To evaluate the phase compositions of the multi-layered Cu/ $\text{Cu}_2\text{O}$  nanostructures, X-ray diffraction (XRD) experiments were carried out on rods that had been deposited on gold substrates to eliminate the diffraction contribution from the copper substrates otherwise used. The diffractograms obtained for 80 nm, 200 nm and 1  $\mu\text{m}$  multi-layered rods are presented in Figure 5 which also contains the diffraction pattern for a 200 nm rod sample annealed at 250 °C. In the diffractograms, all peaks except one for the as deposited samples could be attributed to either Cu, Au or  $\text{Cu}_2\text{O}$  (see Figure 5) and the refined lattice parameters were in good agreement with literature values as can be seen from Table S1 in the Supporting Information. The remaining very small peak around  $2\theta=40^\circ$  can be ascribed to the Au substrate since it was also observed in a diffractogram of an uncoated Au sample. The XRD

results are also in good agreement with those previously obtained<sup>22</sup> after deposition of layers of Cu<sub>2</sub>O and Cu on planar electrodes. The present results thus show that layers containing crystalline Cu and Cu<sub>2</sub>O, respectively, were obtained within the pores of all three templates. As the 200 nm rod sample that had undergone annealing exhibited a diffractogram which was very similar to that obtained for the as prepared 200 nm rod sample, it further suggests that the heat treatment did not give rise to any dramatic change in the Cu<sub>2</sub>O and Cu crystallite sizes. After the heat treatment a set of broad peaks, however, appeared at angles slightly larger than those seen for the Au peaks. These peaks appeared to be due to a cubic phase with a lattice parameter of 4.045(3)Å which suggests that an Au-Cu phase was formed during the heat treatment at 250 °C. This hypothesis is supported by the fact that Madakson *et al.*<sup>40</sup> have shown that Cu and Au interdiffuse readily even at temperatures as low as 150 °C. Although the peaks did not match the low temperature intermetallic phases found in the Cu-Au phase diagram, they still match those expected for a cubic close packed solid solution of Au and Cu which according to Vegard's law, should be composed of about 7% atomic Cu and 93% atomic Au.

The results of the XRD analyses consequently demonstrate that both crystalline copper and cuprous oxide were present in all the specimens although the cuprous oxide peak intensities were notably lower than those for the copper peaks.

### 3.4 Electrochemical characterization in Li-ion batteries

The electrochemical behaviour of the multi-layered micro and nanorods was investigated in lithium-ion batteries since it has been shown<sup>29</sup> that Cu<sub>2</sub>O coated copper nanorods can be used as anodes in such devices. Cyclic voltammograms were recorded for the different samples (i.e. the 80 nm, 200 nm as deposited and heat treated, as well as the 1 µm rods)

versus a lithium counter electrode at scan rates from 0.1 to 100 mV s<sup>-1</sup>. As is evident from Figure 6, which show the first and second cycle voltammograms recorded at a scan rate of 0.1 mV s<sup>-1</sup>, the scans were made from the open circuit potential (OCP), i.e. around 3.15 V vs. Li<sup>+</sup>/Li to 0.05 V vs. Li<sup>+</sup>/Li and back to 3.0 V vs. Li<sup>+</sup>/Li. Since Cu<sub>2</sub>O is known to undergo a conversion reaction according to  $\text{Cu}_2\text{O} + 2 \text{Li}^+ + 2 \text{e}^- = 2 \text{Cu} + \text{Li}_2\text{O}$  with a standard potential of about 2.1 V vs. Li<sup>+</sup>/Li the shapes of the obtained voltammograms are, however, somewhat unexpected since a single Cu<sub>2</sub>O reduction peak and a single oxidation peak would be expected and as the rod based electrodes also exhibited an electroactive potential window covering more than 2 V. We have, however, previously shown<sup>29</sup> that Cu<sub>2</sub>O coated copper nanorods can give rise to similar voltammograms with electroactivity down to about 0.1 V vs. Li<sup>+</sup>/Li as a result of the presence of a distribution of nanoparticles with different sizes and hence redox potentials (the redox potential is expected to become more negative as the particle size decreases<sup>29, 41, 42</sup>). A comparison of the first and second cycle voltammograms indicate that the first reduction charge was larger than the first oxidation charge and consequently also larger than the second reduction charge. Although the formation of a solid electrolyte interface (SEI) layer (as a result of the degradation of the electrolyte) could explain some of the extra reduction charge on the first cycles it is unlikely to be the main factor as the general shape of the first and second cycle voltammograms was very similar. The peak at about 1.15 V vs. Li<sup>+</sup>/Li is in fact the only feature on the first cycle that is likely to have been due to SEI formation. A similar SEI peak was also seen at about 1.1 V vs. Li<sup>+</sup>/Li in a previous study<sup>29</sup> of the electrochemical behaviour of Cu<sub>2</sub>O coated copper nanorods. The voltammograms in Figure 6 hence suggest that the smaller reduction charge on the second cycle mainly was due to an incomplete reformation of the Cu<sub>2</sub>O on the first cycle oxidation scan. For the three as prepared samples two broad oxidation peaks can be seen on both the first and second oxidation scan at about 1.25 and 2.5 V vs. Li<sup>+</sup>/Li, respectively. For the heat treated 200 nm

rod sample the latter oxidation peaks were, however, replaced by two rather well-defined peaks at about 1.9 and 2.3 V vs. Li<sup>+</sup>/Li, respectively. The latter suggests that the oxidation peaks stemmed from the oxidation of a distribution of copper nanoparticles with different sizes (as discussed in more detail in our previous paper <sup>29</sup>) and that the heat treatment gave rise to a more narrow distribution of larger particles. A formation of larger particles during the heat treatment is in fact also supported by a comparison of the SEM images in Figure 2 and 3 with the corresponding SEM image in Figure 2b in reference 29 depicting heat treated Cu<sub>2</sub>O nanorods. The electrochemical behaviour on the first and second cathodic scans was likewise more well-defined for the heat treated 200 nm rod sample as two main reduction peaks were seen at about 1.6 and 1.1 vs. Li<sup>+</sup>/Li, respectively. From the voltammograms it is also evident that the oxidation charge was smaller for the heat treated sample than for the as prepared 200 nm rod sample. This could suggest that the presence of larger particles gives rise to a lower utilization degree of the electroactive material in agreement with previous findings <sup>29</sup>. The lack of a clear reduction peak at about 1.65 V vs. Li<sup>+</sup>/Li for the 80 nm rods could also indicate that smaller Cu<sub>2</sub>O particles were present within these rods as opposed to for the 200 nm and 1 μm rods. This further supported by the finding that the oxidation peak at about 1.25 V vs. Li<sup>+</sup>/Li in fact was larger than that at about 2.5 V vs. Li<sup>+</sup>/Li for the 80 nm rods in contrast to for the 200 nm and 1 μm rods.

In Figure S2 in the Supporting Information it is further demonstrated that the difference between the first reduction peak (e.g. at 1.65 V vs. Li<sup>+</sup>/Li) and the corresponding oxidation peak (e.g. at 2.35 V vs. Li<sup>+</sup>/Li) depended linearly on the logarithm of the peak current for scan rates between 0.1 and 1.6 mV s<sup>-1</sup>. This demonstrates that the potential difference (i.e. the hysteresis) was controlled by an overpotential associated with the electron transfer processes (rather than the iR drop) in good agreement with previous findings <sup>29</sup>. A plot of the peak potential difference versus the peak current is shown in Figure S2. By plotting the peak

current density of the last oxidation peak (positioned at 2.35 V vs. Li<sup>+</sup>/Li on the first scan) as a function of the scan rate and the square root of the scan rate, as is shown in Figures S2b and S2c, respectively, it was found that both approaches gave rise to linear plots. The latter is puzzling as it indicates that the reformation of the Cu<sub>2</sub>O exhibits a mixed semi-infinite diffusion and thin layer cell behaviour. This is also evident from the plots of the logarithm of the peak current versus the logarithm of the scan rate seen Figure S3 in the Supporting Information). This phenomenon could, however, be explained by the Cu<sub>2</sub>O layer on the copper parts of the rods. Since the Cu<sub>2</sub>O layer was about 15 nm thick it can be expected to give rise to a thin-layer like behaviour while a typical semi-infinite response would be expected for the thicker Cu<sub>2</sub>O layers. It should also be pointed out that the diffusion in the present case should be spherical rather than planar which means that an exponent of 0.5 is unlikely to be obtained in Figure S3.

Extensive rate performance testing was further performed at scan rates ranging from 0.1 to 100 mV s<sup>-1</sup> and some selected voltammograms for each sample are presented in Figure 7. It is seen that the shapes of the voltammograms were similar for all the samples, especially at high rates. At 5 mV s<sup>-1</sup>, two reduction and two oxidation peaks could be seen for all rod dimensions (in good agreement with the first cycle voltammograms in Figure 6) while the voltammograms for the highest scan rates e.g. 100 mV s<sup>-1</sup> were more drawn-out and featureless suggesting a pseudocapacitive electrochemical behaviour. A comparison of the results for the as prepared and heat treated 200 nm rod electrodes indicates that the heat treatment gave rise to a decreased electrochemical capacity most likely due to the formation of larger Cu<sub>2</sub>O particles which could not be cycled to the same extent as the smaller particles present in the as deposited sample.

To compare the capacities of the different rod electrodes their reduction and oxidation charges were evaluated for each scan rate. As is seen in Figure 8, the footprint area capacity

was used to compare the samples in the absence and presence of normalization with respect to the effective electrode surface area. The latter area was calculated based on the template pore density and the various rod dimensions obtained from the SEM analyses (see Table S2 in the Supporting Information). For all electrodes, a dramatic drop in the capacity was found when increasing the scan rate from 0.1 to about 2  $\text{mV s}^{-1}$  after which drop in capacity with increasing scan rate was relatively small. The maximum area normalized capacity, which was obtained at a scan rate of 0.1  $\text{mV s}^{-1}$ , was also found to be comparable for all the electrodes. The latter is surprising considering that the theoretical capacity for the sample with 1  $\mu\text{m}$  rods should have been approximately three times larger than that for the 200 nm rod electrode and about 10 times larger than for the 80 nm rod electrode (see Table S2). These results hence clearly demonstrate that only a fraction of the total amount of  $\text{Cu}_2\text{O}$  present within the 1  $\mu\text{m}$  rod electrode could be accessed during these experiments. This suggests that the capacity originated from an electroactive layer of  $\text{Cu}_2\text{O}$  in contact with the electrolyte and that the thickness of this layer depended on the time domain of the measurements (i.e. the scan rate employed).

As is seen in Figure S4 in the Supporting Information the cyclic voltammogram recorded for the Cu substrate (at a scan rate of 0.1  $\text{mV s}^{-1}$ ) exhibited the same general features as seen in Figure 6 for the rod based electrodes although there was still a large mismatch between the reduction (21  $\mu\text{Ah cm}^{-2}$ ) and oxidation charge (6  $\mu\text{Ah cm}^{-2}$ ) on the fourth cycle. The latter mismatch (which could have been due to the presence of a thicker oxide layer) was clearly not seen for the rod based electrodes. It is therefore reasonable to assume that the steady state capacity of the Cu substrate would be somewhat lower than 6  $\mu\text{Ah cm}^{-2}$ . This hypothesis is also in agreement with the expected value as is described below. Since the 200 nm nanorod electrode provided a capacity of about 32  $\mu\text{Ah cm}^{-2}$  for an estimated total surface area of about 10  $\text{cm}^2$  (see Table S2) it can be estimated that the contribution from the Cu substrate

should have been about  $5 \mu\text{Ah cm}^{-2}$  after correction for the fact that only about  $3 \mu\text{m}$  of the total length of the rods of approximately  $5 \mu\text{m}$  was due to  $\text{Cu}_2\text{O}$ . Similar results were also obtained for the  $80 \text{ nm}$  and  $1 \mu\text{m}$  rod electrodes. In our previous work<sup>29</sup> we have likewise shown that capacities of up to  $265 \mu\text{Ah cm}^{-2}$  can be obtained with  $\text{Cu}_2\text{O}$  coated  $\text{Cu}$  nanorod ( $200 \text{ nm}$  diameter) electrodes having an average geometrical areal gain factor of 60. Based on the latter values the  $\text{Cu}$  substrate would be expected to exhibit a capacity of about  $4 \mu\text{Ah cm}^{-2}$  in good agreement with the values above. These results consequently show that the relatively low capacities obtained here in comparison with those previously obtained for  $\text{Cu}_2\text{O}$  coated copper nanorod electrodes<sup>29</sup> merely stem from the lower average geometrical areal gain factors of the present electrodes.

One important question which could not be addressed in our previous work<sup>29</sup> is whether the capacity of a  $\text{Cu}_2\text{O}$  rod based electrode can be increased by increasing the diameter of the rod (i.e. if all of the  $\text{Cu}_2\text{O}$  in the rods remain electroactive when increasing the diameter of the rods). This question can, however, be addressed based on the present data as is described below. To estimate the thickness of the electroactive layer of  $\text{Cu}_2\text{O}$  the following approach was employed. As previous results have indicated that the electroactive  $\text{Cu}_2\text{O}$  layer should be at least  $15 \text{ nm}$  thick<sup>29</sup> it was assumed that the entire volume of the  $80 \text{ nm}$  rods was electroactive at the lowest scan rate, i.e.  $0.1 \text{ mV s}^{-1}$ . This assumption is supported by the fact that the capacity of  $21 \mu\text{Ah cm}^{-2}$  found for the  $80 \text{ nm}$  rod electrode agreed well with the theoretical value of  $19 \mu\text{Ah cm}^{-2}$  obtained with the data presented in Table S2. Based on these assumptions and the normalized capacity data presented in Figure 8, the thickness of the electroactive  $\text{Cu}_2\text{O}$  layer was found to be approximately  $30$ ,  $23$  and  $25 \text{ nm}$  for the  $200 \text{ nm}$ ,  $200 \text{ nm}$  heat treated and  $1 \mu\text{m}$  rod electrodes, respectively, for a scan rate of  $0.1 \text{ mV s}^{-1}$ . The present results consequently suggest that the thickness of the electroactive  $\text{Cu}_2\text{O}$  layer was about  $20$  to  $40 \text{ nm}$  thick at a scan rate of  $0.1 \text{ mV s}^{-1}$  and that the thickness of the layer

decreased with increasing rod diameter and after heat treatment. Given the fact that the normalized capacity for the 80 nm rod electrode was approximately four times lower at the 5 mV s<sup>-1</sup> scan rate than at 0.1 mV s<sup>-1</sup> rate, the electroactive layer thickness should only have been about 5 nm thick at the higher scan rate (similar results were likewise obtained for the 200 nm and 1 μm rod electrodes). This dramatic decrease in the thickness of the electroactive layer explains the shape of the capacity versus scan rate plots in Figure 8. For even higher scan rates the electrochemical reactions can therefore be described based on a surface immobilized electroactive layer of Cu<sub>2</sub>O which also explains the pseudocapacitive shaped voltammograms seen at the higher scan rates. The capacity for the highest scan rates should hence be composed of a contribution from a thin electroactive Cu<sub>2</sub>O layer and the ubiquitous contribution from the Cu<sub>2</sub>O present on the copper segments. The present behaviour is in fact similar to that found for TiO<sub>2</sub> for which similar plots of the capacity as a function of the scan rate have been found. In the latter case it has been proposed that TiO<sub>2</sub> films with thicknesses of up to about 17 nm can be cycled reversibly even at relatively high scan rates<sup>43</sup>.

As indicated above it is reasonable to assume that the capacity of the electrodes were limited by the oxidation of the copper nanoparticles generated in the conversion reaction. Since the oxidation (i.e.  $2 \text{ Cu} + \text{Li}_2\text{O} = \text{Cu}_2\text{O} + 2 \text{ Li}^+ + 2 \text{ e}^-$ ) starts at the interface between the electrode and the electrolyte and continues at the inward moving interface between the Cu<sub>2</sub>O layer and the copper nanoparticle/Li<sub>2</sub>O matrix, the rate of the reaction should become limited by the transport of lithium ions through the growing Cu<sub>2</sub>O layer. This means that the oxidation current should decrease with time as the thickness of the Cu<sub>2</sub>O layer increases. The oxidation thus leads to the formation of a passivating Cu<sub>2</sub>O layer on top of the remaining copper nanoparticle/Li<sub>2</sub>O matrix which is likely to prevent the attainment of a complete oxidation of the copper nanoparticles generated during the preceding reduction step. The rate limiting factor during the reduction of the Cu<sub>2</sub>O (i.e.  $\text{Cu}_2\text{O} + 2 \text{ Li}^+ + 2 \text{ e}^- = 2 \text{ Cu} + \text{Li}_2\text{O}$ ) is

instead likely to be the formation of a thicker layer of the copper nanoparticle/Li<sub>2</sub>O layer on the remaining Cu<sub>2</sub>O. Since the diffusion rate of lithium ions in a matrix of copper nanoparticles and Li<sub>2</sub>O should be relatively high it is likely that the reduction of the Cu<sub>2</sub>O should be more complete than the subsequent oxidation. As is clearly shown by the experimental data, only a fraction of the Cu<sub>2</sub>O present within the 200 nm and 1 μm rods was, nonetheless, reduced on the first cycle indicating that it is still very difficult to fully reduce sufficiently thick layers of Cu<sub>2</sub>O. These present results thus clearly show that it is challenging to increase the capacity of Cu<sub>2</sub>O based electrodes by increasing the thickness of the Cu<sub>2</sub>O layer and that the thickness of the electroactive layer most likely is determined by the transport rate of lithium ions through the growing Cu<sub>2</sub>O layer during the oxidation step.

Based on the experimental results it is in fact possible to obtain an estimate of the diffusion coefficient,  $D$ , for the diffusion of lithium ions through the Cu<sub>2</sub>O layer. As described above the thickness of the electroactive layer was about 40 nm at a scan rate of 0.1 mV s<sup>-1</sup> while it was about 5 nm for a scan rate of 5 mV s<sup>-1</sup>. For scan rates of 0.2 and 0.8 mV s<sup>-1</sup> the corresponding values were found to be about 28 and 18 nm. By plotting the thickness of the electroactive layer (i.e.  $\Delta$ ) as a function of the square root of the time, (calculated based on the scan rate and an assumed potential window of 2 V) available for the diffusion, a linear relationship was obtained for these three points by employing the well-known equation  $\Delta = (2Dt)^{0.5}$ <sup>44</sup>, as can be seen in Figure S3 in the supporting information. From the slope of this line a diffusion coefficient of about  $2 \cdot 10^{-16}$  cm<sup>2</sup> s<sup>-1</sup> was obtained. A similar value was likewise obtained merely by assuming an electroactive layer thickness of 40 nm for a scan rate of 0.1 mV s<sup>-1</sup> and a potential window of 2.0 V. This very low diffusion coefficient indicates that the lithium ions interact significantly with the O<sup>2-</sup> ions during their passage through the Cu<sub>2</sub>O layer.

As is seen in Figure 9 (which shows the area based capacity as a function of the cycle number for galvanostatic cycling of the electrodes between 0.05 and 3 V vs. Li<sup>+</sup>/Li using a current density of 30  $\mu\text{A cm}^{-2}$ ) the long-time cycling behaviour of the rod based electrodes was also studied using the Li-ion approach. The 200 nm rod electrode exhibited the highest area based capacity while the lowest values were found for the 80 nm and 1  $\mu\text{m}$  rod electrodes in good agreement with the voltammetric results in Figure 8 and the active electrode areas presented in Table S2. It is also seen that the heat treatment of the 200 nm rod electrodes gave rise to a decreased areal capacity. Since the voltammetric results suggest that the heat treatment gave rise to an increased crystallite size, it is reasonable to assume that the capacity decrease was connected to the increase in the latter.

In Figure 9 it is likewise seen that the area based capacity increased significantly upon cycling and that the reduction charge generally was larger than the oxidation charge. The latter supports the hypothesis that the oxidation reaction was the capacity limiting step. As has been described previously<sup>29</sup> the increased capacity with increasing cycle number can be explained by the electromilling effect associated with the conversion reaction. Since the experiments were performed at a rate of about 0.6C for the 80 nm rods, which roughly corresponds to the time domain of the 0.8  $\text{mV s}^{-1}$  cyclic voltammograms it is unlikely that the full capacity was attained during the initial cycles. The increase in the capacity upon the cycling could then be explained by the electromilling generating smaller particles which allowed a better access to the total amount of the  $\text{Cu}_2\text{O}$  as well as an increase in the contribution from double layer charging.<sup>29</sup> It should be noted that the largest increase in the capacity during the first 10 cycles was seen for the heat treated 200 nm rod electrode which should have contained the largest particles. These results therefore support the hypothesis that the thickness of the electroactive layer also depends on the particle size. One explanation for

this could be that the  $\text{Li}^+$  diffusion rate through the  $\text{Cu}_2\text{O}$  layer increases with increasing number of grain boundaries (i.e. with decreasing particle size).

#### 4. Conclusions

Freestanding nano- and microrods composed of stacked layers of copper and cuprous oxide with thicknesses between 125 and 500 nm have been fabricated using a straightforward one-step template-assisted pulsed galvanostatic electrodeposition approach. As the thickness of the individual layers readily can be controlled by varying the current density and the pulse time the approach provides new possibilities for inexpensive and fast manufacturing of  $\text{Cu}_2\text{O}/\text{Cu}$  multi-layered rod structures. The presence of the multilayers within the rods has been verified by SEM, EDS, XRD, TEM and EELS investigations and it was found that the thickness of the  $\text{Cu}_2\text{O}$  and Cu layers depended on the properties of the templates used via the current density obtained within the pores of the template during the deposition.

The electrochemical performance of electrodes composed of freestanding rods with diameters of 80 nm, 200 nm and 1  $\mu\text{m}$ , respectively, was compared in Li-ion batteries based on the following conversion reaction:  $\text{Cu}_2\text{O} + 2 \text{Li}^+ + 2 \text{e}^- = 2 \text{Cu} + \text{Li}_2\text{O}$ . The results clearly show that the electrodes exhibited a potential window of more than 2 V, an effect which was ascribed to the presence of a distribution of  $\text{Cu}_2\text{O}$  (and Cu nanoparticles, respectively) with different sizes and redox potentials.

The fact that approximately the same areal capacity was obtained independent of the diameter of the multi-layered rods after correction for the active areas of the electrode, further demonstrate that the major part of the  $\text{Cu}_2\text{O}$  present within the layers of the 1  $\mu\text{m}$  rod electrode was inactive at scan rates of 0.1  $\text{mV s}^{-1}$ . The results indicate the presence of an

electroactive layer with a thickness of between 40 and 20 nm for the different electrodes at a scan rate of  $0.1 \text{ mV s}^{-1}$ .

While the thickness of the electroactive layer was found to decrease rapidly when the scan rate was increased from  $0.1$  to  $2 \text{ mV s}^{-1}$ , there was only a marginal decrease when the scan rate was further increased to  $100 \text{ mV s}^{-1}$ . This behaviour (and the presence of an electroactive layer with time domain dependent thickness) can be explained by assuming that the oxidation capacity is limited by the lithium ion diffusion rate through the  $\text{Cu}_2\text{O}$  layer generated during the oxidation step. At a sufficiently high scan rate the electroactive layer hence collapses into a thin layer with a thickness that subsequently is almost independent of further increases in the scan rate. Although the redox reactions are the same independent of the time scale of the experiments, different types of voltammetric or chronopotentiometric responses can thus be obtained depending on the thickness of the electroactive layer.

The present results indicate that  $\text{Cu}_2\text{O}$  based electrodes should be made in the form of e.g.  $50 \text{ nm}$  thick  $\text{Cu}_2\text{O}$  layers on three-dimensional (Cu) current collectors and that the  $\text{Cu}_2\text{O}$  particle size should be as small as possible. Increases in the capacity as a function of the cycle number can also be seen as a result of the electromilling effect associated with the conversion reaction. This capacity increase, which corresponds to an increase in the electroactive layer thickness, could be a result of the increased number of grain boundaries facilitating the  $\text{Li}^+$  diffusion through the  $\text{Cu}_2\text{O}$  layer formed during the oxidation step. The electrochemical performance of present type of 3-D multi-layered rods consequently provides new insights into the electrochemical phenomena limiting the energy and power densities for conversion reaction materials such as  $\text{Cu}_2\text{O}$ .

## 5. Acknowledgements

The authors would like to express their gratitude to Ugo Lafont for the preliminary TEM study and to Linus von Fieandt for valuable discussions regarding the TEM analyses. Henrik Eriksson and Victoria Sternhagen are also acknowledged for technical assistance. Financial support from The Swedish Research Council (VR. 2011–3506 and 2012–4681), The Swedish Energy Agency (STEM), Ångström Advanced Battery Center (ÅABC) and StandUp for Energy is also gratefully acknowledged. The Knut and Alice Wallenberg (KAW) Foundation is acknowledged for providing the electron microscopy facilities at Stockholm University.

## References

1. U. Helmerson, S. Todorova, S. A. Barnett, J-E. Sundgren, L. C. Markert and J. E. Greene, *J. Appl. Phys.*, 1987, **62**, 481-484.
2. G. Binasch, P. Grünberg, F. Saurenbach and W. Zinn, *Phys. Rev. B*, 1989, **39**, 4828-4830.
3. M. N. Baibich, J. M. Broto, A. Fert, F. Nguyen van Dau, F. Petroff, P. Etienne, G. Creuzet, A. Friederich and J. Chazelas, *Phys. Rev. Letters*, 1988, **61**, 2472-2475.
4. H. El Fanity, K. Rahmouni, M. Bouanani, A. Dinia, G. Schmerber, C. Mény, P. Panissod, A. Cziraki, F. Cherkaoui and A. Berrada, *Thin Solid Films*, 1998, **318**, 227-230.
5. H. Pan and Y-W. Zhang, *Nano Energy*, 2012, **1**, 488-493.
6. W. Wei, H. Jha, G. Yang, R. Hahn, I. Paramasivam, S. Berger, E. Spiecker and P. Schmuki, *Adv. Mat.*, 2010, **22**, 4770-4774.
7. P. E. Hovsepian, D. B. Lewis, W-D. Müünz, A. Rouzaud and P. Juliet, *Surf. Coat. Tech.*, 1999, **116-119**, 727-734.
8. P. E. Hovsepian, D. B. Lewis, W-D. Müünz, S. B. Lyon and M. Tomlinson, *Surf. Coat. Tech.*, 1999, **120-121**, 535-541.
9. T. Hurkmans, T. Trinh, D. B. Lewis, J. S. Brooks and W-D. Müünz, *Surf. Coat. Tech.*, 1995, **76-77**, 159-166.
10. M. Nordin, M. Larsson and S. Hogmark, *Surf. Coat. Tech.*, 1998, **106**, 234-241.
11. M. Setoyama, A. Nakayama, M. Tanaka, N. Kitagawa and T. Nomura, *Surf. Coat. Tech.*, 1996, **86-87**, 225-230.
12. M. Alper, P. S. Alpin, K. Attenborough, D. J. Dingley, R. Hart, S. J. Lane, D. S. Lashmore and W. Scharzacher, *J. Magn. Magn. Mater.*, 1993, **126**, 8-11.
13. J. Eskhult, M. Herranen and L. Nyholm, *J. Electroanal. Chem.*, 2006, **594**, 35-49.
14. C. P. Oliveira, R. G. Freitas, L. H. C. Mattoso and E. C. Pereira, in *Nanostructured materials in Electrochemistry*, ed. A. Eftekhari, Wiley-VCH, 2008, p. 158.
15. K. Edström, D. Brandell, T. Gustafsson and L. Nyholm, *Electrochem. Soc. Interface*, 2011, **20**, 41-46.
16. T. Pauporte, A. Goux, A. Kahn-Harari, N. De Tacconi, C.R. Chenthamarakshan, K. Rajeshwar and D. Lincot, *J. Phys. Chem. Solids*, 2003, **64**, 1737-1742.
17. F. Erler, C. Jakob, H. Romanus, L. Spiess, B. Wielage, T. Lampke and S. Steinhauser, *Electrochim. Acta*, 2003, **48**, 3063-3070.
18. J.A. Switzer, C- Hung, L-Y. Huang, E.R. Switzer, D.R. Kammler, T.D. Golden and E.W. Bohannon, *J. Am. Chem. Soc.*, 1998, **120**, 3530-3531.
19. S. M. Cox, U. Happek, D. Banga, M. K. Mathe and J. L. Stickney, *Langmuir*, 2006, **22**, 10590-10595.
20. B. W. Gregory and J. L. Stickney, *J. Electroanal. Chem.*, 1991, **300**, 543-561.
21. M. Lakatos-Varsanyi, A. Miko, L.K. Varga and E. Kalman, *Corros. Sci.*, 2005, **47**, 681-693.
22. J. Eskhult and L. Nyholm, *J. Electrochem. Soc.*, 2008, **155**, D115-D122.
23. C-O. A. Olsson and D. Landolt, *Electrochim. Acta*, 2003, **48**, 1093-1104.
24. E. D. Mishina, K. Nagai and S. Nakabayashi, *Nano Letters*, 2001, **1**, 401-404
25. Y. Mao, J. He, X. Sun, W. Li, X. Lu, J. Gan, Z. Liu, L. Gong, J. Chen, P. Liu and Y. Tong, *Electrochim. Acta*, 2012, **62**, 1-7.
26. M. Valvo, M. Roberts, G. Oltean, B. Sun, D. Rehnlund, D. Brandell, L. Nyholm, T. Gustafsson and K. Edström, *J. Mater. Chem. A*, 2013, **1**, 9281-9293.
27. J. Cabana, L. Monconduit, D. Larcher and M.R. Palacín, *Adv. Enrgy Mater.*, 2010, **22**, E170-E192.
28. J.W. Long, B. Dunn, D.R. Rolison and H.S. White, *Chem. Rev.*, 2004, **104**, 4463-4492.
29. M. Valvo, D. Rehnlund, U. Lafont, M. Hahlin, K. Edström and L. Nyholm, *J. Mater. Chem. A*, 2014, **2**, 9574-9586.

30. S. Leopold, I. U. Schuchert, J. Lu, M. E. Toimil Molares, M. Herranen and J. O. Carlsson, *Electrochim. Acta*, 2002, **47**, 4393-4397.
31. J. A. Switzer, H. C-J, E. W. Bohannan, M. G. Shumsky, T. D. Golden and D. C. Van Aken, *Adv. Mater.*, 1997, **9**, 334-338.
32. Y. C. Zhou and J. A. Switzer, *Mater. Res. Innov.*, 1998, **2**, 22-27.
33. E. W. Bohannan, H. L-Y, F. S. Miller, M. G. Shumsky and J. A. Switzer, *Langmuir*, 1999, **15**, 813-818.
34. J. Eskhult, C. Ulrich, F. Björefors and L. Nyholm, *Electrochim. Acta*, 2008, **53**, 2188-2197.
35. H. Ju, J.K. Lee, J. Lee and J. Lee, *Curr. App. Phys.*, 2012, **12**, 60-64.
36. S. Kenane and L. Piraux, *J. Mater. Res.*, 2002, **17**, 401-406.
37. S. Nakanishi, in *Nanostructured materials in Electrochemistry*, ed. A. Eftekhari, Wiley-VCH, 2008, p. 283.
38. M. Fujita, Y. Miyakita, N. Sogoshi, S. Nakabayashi and M. Ishii, *Transactions of the Materials Research Society of Japan*, 2005, **30**, 1041-1044.
39. B. S. Unitcell, 2000.
40. P. Madaksson and J.C. Liu, *J. Appl. Phys.*, 1990, **68**, 2121-2126.
41. R.A. Masitas and F.P. Zamborini, *J. Amer. Chem. Soc.*, 2012, **134**, 5014-5017.
42. P.L. Redmond, A.J. Hallock and L.E. Brus, *Nano Letters*, 2005, **5**, 131-135.
  
43. R. van de Krol, A. Goossens and J. Schoonman, *J. Phys. Chem. B*, 1999, **103**, 7151-7159.
44. A. J. Bard and L. R. Faulkner, in *Electrochemical Methods*, Wiley, 2nd edn., 2002, p. 147.

## Figure captions

Graphical abstract:

Schematic representation of multilayered Cu/Cu<sub>2</sub>O nanostructures electrodeposited in a porous polycarbonate membrane and a micrograph of the obtained rods.

Figure 1: Chronopotentiograms recorded during the Cu/Cu<sub>2</sub>O multilayer electrodepositions. While a set of short cathodic current pulses with current densities between 0.1 mA cm<sup>-2</sup> and 1.0 mA cm<sup>-2</sup> were used to deposit Cu<sub>2</sub>O, longer pulses with a current density of 10 mA cm<sup>-2</sup> were utilized for the copper deposition. The depositions were carried out with templates having nominal pore diameters of 80 nm (black curve), 200 nm (red curve) and 1 μm (blue curve), respectively.

Figure 2: SEM micrographs of the multilayered rods deposited with the a) 80 nm template, b) 200 nm template and c) 1 μm template. Notice the ‘bamboo-like’ morphology for the 1 μm and 200 nm rods.

Figure 3: Micrograph depicting a detached multilayered rod with a diameter of 1 μm (a) where the position of an EDS line scan performed over four layer interfaces has been indicated. The associated EDS line scans for Cu (L-line) and O (K-line) spectra (b). Comparative images of the multilayers of a rod with a diameter of 1 μm obtained with a secondary electron detector (c) and an in-lens backscattered electron detector (d).

Figure 4: Bright field TEM (a) and HAADF-STEM (b) images of multilayered Cu/Cu<sub>2</sub>O nanorods with a diameter of about 80 nm. The HAADF-STEM image (b) shows a magnification of the three bottom nanorods displayed in (a). The HAADF-STEM image in (c) shows the layer interphase of a selected nanorod. The red rectangle indicates the region used in the EELS mapping. The oxygen and copper concentration maps (d) obtained from the EELS mapping of the rod in (c).

Figure 5: X-ray powder diffraction patterns for multilayered Cu/Cu<sub>2</sub>O rods deposited on gold substrates. The diffraction patterns were collected for rods with diameters of 80 nm, 200 nm and 1 μm, respectively. The 200 nm HT pattern was obtained for 200 nm rods annealed at 250°C in vacuum.

Figure 6: First and second cycle cyclic voltammograms recorded for the as-synthesized rods with diameters of 80 nm (a), 200 nm (b) and 1 μm (c), respectively, using a scan rate of 0.1

$\text{mV s}^{-1}$  and potentials between 0.05 and 3.0 V (vs.  $\text{Li}^+/\text{Li}$ ). The corresponding voltammograms obtained for the heat treated 200 nm sample are depicted in (d).

Figure 7: Cyclic voltammograms recorded at scan rates between 10 and 100  $\text{mV s}^{-1}$  for rods with diameters of 80 nm (a), 200 nm (b), 1  $\mu\text{m}$  (c) as well as for the heat treated 200 nm rods (d). The insets depict the corresponding voltammograms obtained at a scan rate of 5.0  $\text{mV s}^{-1}$ .

Figure 8: The footprint areal capacity (left axis) and the footprint area capacity normalized with respect to the electrode surface area (right axis) as a function of the scan rate for the rods with diameters of 80 nm (a), 200 nm (b), 1  $\mu\text{m}$  (c) as well as for the heat treated 200 nm rods (d). The capacities were calculated from the voltammograms depicted in Figure 7. The open and filled symbols denote to the reduction and oxidation based capacities, respectively.

Figure 9: The footprint areal capacity as a function of the cycle number for galvanostatic cycling of multilayered rods with diameters of 80 nm, 200 nm and 1  $\mu\text{m}$ , respectively. The corresponding curve for the heat treated 200 nm rods has also been included for comparison. The current density used was 30  $\text{mA cm}^{-2}$  and the open and filled symbols denote to the oxidation and reduction based capacities, respectively.